PERGAMON International Journal of Multiphase Flow 25 (1999) 1129–1160

International Journal of Multiphase Flow

www.elsevier.com/locate/ijmulflow

# Shape of long bubbles in horizontal slug flow

J.R. Fagundes Netto, J. Fabre*, L. Peresson

*Institut de Mécanique des Fluides de Toulouse, UMR CNRS-INP-UPS 5502, Allée du Professeur Camille Soula, 31400 Toulouse, France*

Received 28 December 1998; received in revised form 14 April 1999

It is a pleasure for us to dedicate this paper to Professor Gad Hetsroni on the occasion of his birthday. His magnificent task at the editorship of the *International Journal of Multiphase Flow* has been decisive for the development and the dissemination of the scientific results of our community. Happy birthday Gad.

**Abstract**

This paper presents a theoretical and experimental study of the shape of long isolated bubbles similar to those observed in horizontal slug flows. Bubbles of different volumes were studied, their lengths varying from 30 to 100 times the pipe diameter. Two different shapes were observed corresponding to plug and slug flow regimes. The transition between plug and slug flow was shown to depend on both Froude number and bubble length. A model based on the mass and momentum conservation equations of each phase is proposed. It is able to predict the transition between plug and slug flow regimes as well as the volume and the shape of long bubbles. It is shown that usual slug flow codes that aim to predict the void fraction tend to overestimate the gas fraction in the bubble region. The model may be easily implemented into slug tracking codes. © 1999 Elsevier Science Ltd. All rights reserved.

*Keywords:* Two-phase flow; Slug flow; Plug flow; Bubble shape; Flow pattern; Transition

## 1. Introduction

Horizontal slug flow has been the object of studies for at least 30 years. Models to predict the phase velocities and pressure gradient were developed, based on the unit cell concept initially described by Wallis (1969). Dukler and Hubbard (1975) proposed the first comprehensive model and further papers were variations upon the same concept. Fabre et al.

* Corresponding author. Tel.: +33-5-6128-5853; fax: +33-5-6128-5899.
*E-mail address:* fabre@imft.fr (J. Fabre)

0301-9322/99/$ - see front matter © 1999 Elsevier Science Ltd. All rights reserved.
PII: S0301-9322(99)00041-5

(1989) proposed a different approach based on a statistical cell unit (see also Fabre and Liné, 1992). All these developments improved the ability to predict some important flow parameters such as pressure gradient, mean phase velocities and mean volume fractions. But in no way did they improve the knowledge of the slug structure itself, i.e., very little advance was made on the prediction of the statistics of bubble and slug lengths and their evolution along the pipe.

Gas–liquid slug flow is formed by an alternation in space and time of long bubbles and liquid slugs, as shown in Fig. 1. In the unit cell models, the gas volume fraction in the bubble region is usually determined, assuming that the liquid film has a constant thickness like in fully developed stratified flow. It is also assumed that bubbles and slugs have constant lengths, which leads to a periodic flow structure. In the statistical cell model the hypothesis is less restrictive. The structure is not necessarily periodic, although it is also assumed that the liquid films are fully developed. From various experiments carried out in horizontal flow, the gas volume fraction in any section of the bubble region depends on the distance to the bubble nose. Moreover, the resulting structure is never periodic. In reality, the probability density function (PDF) of the bubble and slug lengths are widely distributed about the average (see Fig. 2), as observed by Grenier (1997). It is shown that bubbles measuring from 5 to 50$D$ were observed, whereas the slug length was observed in the range between 5 and 30$D$.

Some interesting experimental works were made recently by Dhulesia et al. (1991), Nydal et al. (1992) and Grenier (1997), who provided a statistical description of slug flows. Recent attempts to predict the evolution of the slug structure were made using two different approaches. The first and also the most widely employed approach is the 'slug-tracking' method, where the volume and position of each individual bubble and slug are followed step-by-step along the pipe. The bubbles are allowed to expand as pressure decreases and coalescence may occur. Straume et al. (1992), Barnea and Taitel (1993) and Nydal and Banerjee (1995) applied this method to describe the slug flow evolution along the pipe. The second approach aims at solving transport equations for the distribution of bubble and slug lengths. The first attempt to use this method was made by Grenier (1997). It was limited to the pipe region, where the interaction between bubbles is supposed weak and the depressurization is the only cause of structure evolution. In any of the proposed methods, additional closure laws are required to provide unknown relations such as the length of a bubble as a function of its volume. Most slug tracking models assume that all bubbles are fully developed, and it will be shown that this assumption leads to large errors, when the bubble length is smaller than 100$D$. Another frequent simplification for horizontal flow assumes that the liquid film is

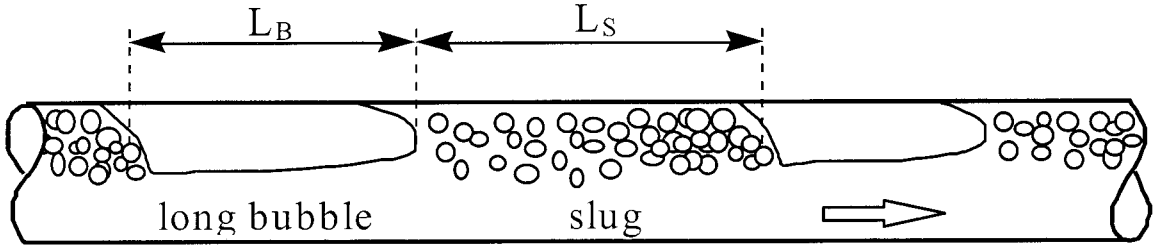


Fig. 1. Gas–liquid horizontal slug flow.

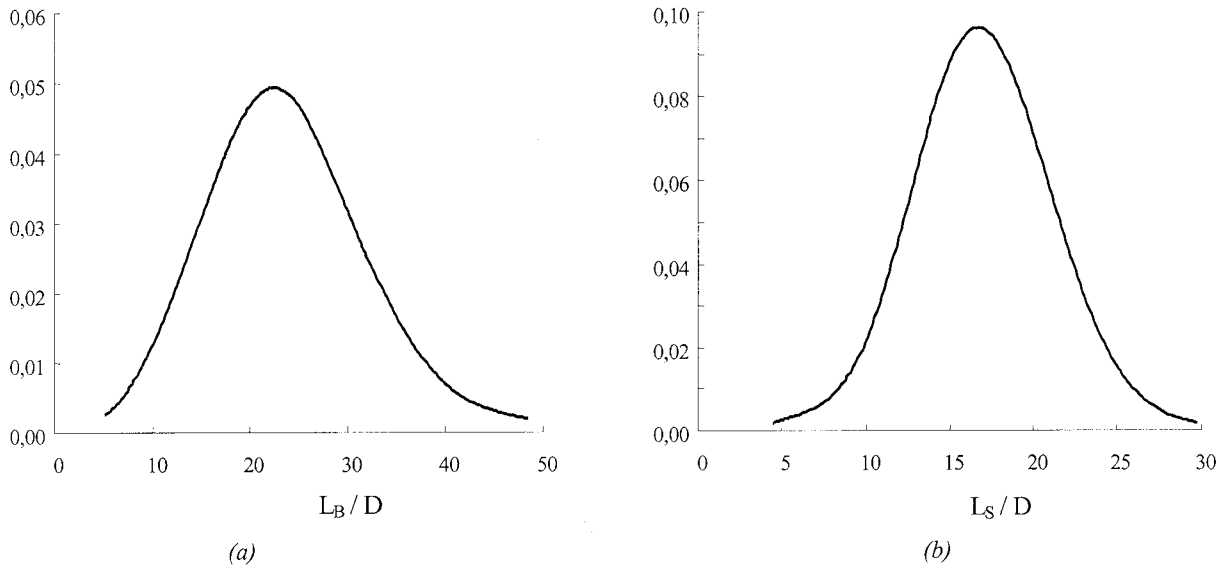


Fig. 2. Lengths probability density functions (PDF), after Grenier (1997); $j_L = j_G = 1.0$ m/s; $D = 53$ mm; measured at 84 m from inlet: (a) long bubble, (b) liquid slug.

motionless under the bubble. This leads to errors in the liquid fraction under a fully developed bubble of at least 5% for air and water at atmospheric condition.

This paper investigates the shape and volume of bubbles of given length as functions of fluid velocity and properties. Grenier et al. (1997) showed that the shape of a bubble depends on the mixture velocity, in agreement with the observations of Woods and Hanratty (1996). This confirms in slug flow, the earlier study of Bendiksen (1984) on isolated bubble that showed that their shape depends on liquid velocity. As shown in Fig. 3, the shape is also independent of the bubble length. These results prove that the flow ahead of the bubble is responsible for

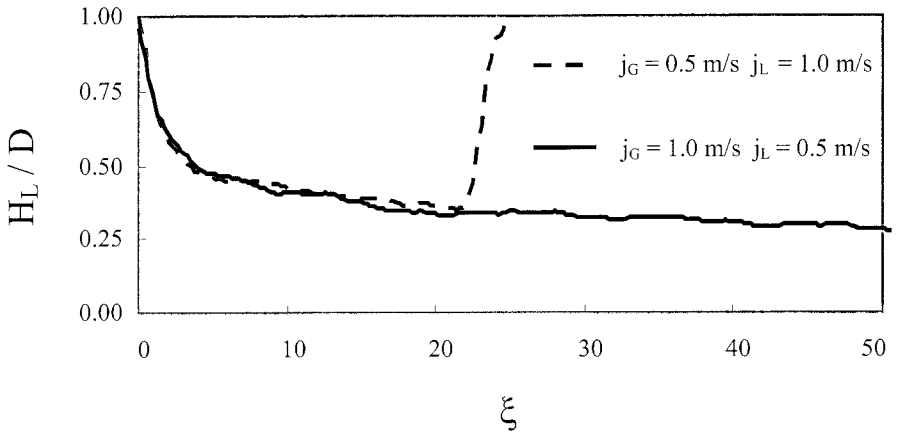


Fig. 3. Shape of two bubbles at the same mixture velocity, after Grenier et al. (1997).

its shape. Studying the behaviour of isolated bubbles in a liquid flow was chosen to ensure a better control of the experiment, so as to avoid the overlap of different phenomena induced by a train of bubbles.

The paper is organised as follows: Section 2 presents the experimental facility which allows the injection of a single bubble without disturbing the liquid flow and describes the sensors used to measure the bubble shape. In Section 3, some preliminary experimental results are presented: the influence of the flow velocity and of the bubble volume on its shape is analysed. In Section 4, a model is proposed: the bubble is divided in four regions, the nose, the body, the hydraulic jump at the back and the tail. After validation, the model is used in the last part of the paper to estimate errors due to the assumption of constant film thickness.

## 2. Experimental facility

The test facility was designed and built at the Institut de Mécanique des Fluides de Toulouse (IMFT) to study the structure of the horizontal slug flow and its evolution along the pipe (Grenier et al., 1997). Air and water are injected in a horizontal 90 m long transparent PVC pipe with an internal diameter of 53 mm. The water flows in a closed loop and a pump provides superficial liquid velocities up to 2.0 m/s. The liquid flow rate is measured by a set of orifice plates and the flow is controlled through electrical valves by the Control and Data Acquisition System (CDAS). The pipe inlet is designed to prepare an air bubble of a given volume and to introduce it in the liquid flow.

Fig. 4 presents a scheme of the test facility. Liquid is supplied at the pipe inlet through the inclined branch 'A'. A predetermined air volume is initially introduced in the vertical branch, where the pneumatic valve 'B' is kept closed. Controlled by the CDAS, valve 'B' opens at the same time that valve 'A' closes. This ensures a constant flow within the horizontal pipe. The liquid flow is deviated into the vertical branch and it pushes the gas volume into the pipe. At a

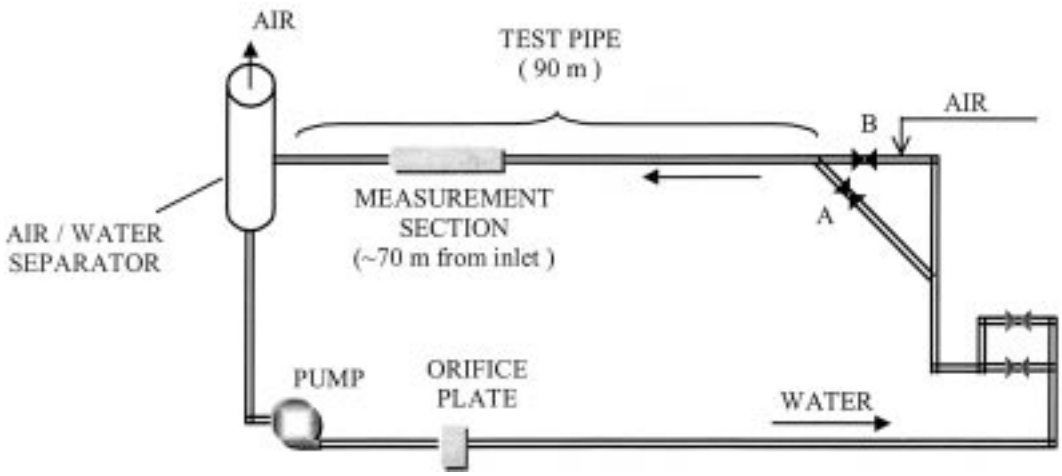


Fig. 4. Test loop scheme.

few meters from the inlet, the gas bubble has already reached its final shape and it travels along the pipe at a rather constant velocity.

The measurement section is placed at 70 m from the inlet. A set of five sensors, further referred to as 'wire probes', is used. The distance between each probe is 1 m. Each sensor consists of a metallic wire electrically isolated by a Teflon layer. The isolated wire, with an external diameter of 0.29 mm is installed vertically at the centreline of the pipe section. The capacitance of the wire is linearly proportional to the height of the liquid around it. An electronic device converts the wire capacitance into a voltage signal. Data from the five sensors allow the determination of the bubble velocity, length and shape. Further details on mounting and calibration procedure of wire probes may be found in (Fagundes Netto, 1999).

These liquid height sensors have been successfully used in the past to characterise the wavy surface of stratified flows. For slug flow condition, however, the liquid reaches the top of the pipe and an extra care is required in the wire mounting. The present installation was designed to avoid water leakage at the top, that could be responsible of overestimating the liquid height. It was impossible, however, to avoid a minimum space of about 1 mm between the seal and the inner pipe wall. At high velocities the liquid trapped in this space may lead to an overestimation on the liquid height, of up to $0.02D$.

The time trace of the measured liquid height is transformed in a space evolution by multiplying the time series by the bubble nose velocity. The liquid height is converted into volume fraction assuming that the gas–liquid interface in the cross section is horizontal. The relations among the geometric parameters in a circular cross section are described in Appendix A. The bubble shape is represented in this paper by the plot of the liquid volume fraction $\alpha_L$ as a function of the distance $\xi$ to the nose of the bubble, measured in pipe diameters.

A conductive sensor was used to validate the wire signal. It is composed of two metallic rings flush mounted at the pipe wall and distant 5 cm from each other. This sensor, further referred to as 'ring probe', measures the electric conductance, that is proportional to the volumetric liquid fraction within the control volume between the two rings. The method was used and discussed by Nydal and Andreussi (1991).

The accuracy in determining the bubble velocity depends on the accuracy in the estimation of the time $\Delta t$ elapsed between the passage of the bubble nose by two successive wires. The uncertainty on $\Delta t$ is equal to the sampling period $1/Fe$, where $Fe$ is the sampling frequency. Thus, the uncertainty $\delta V$ is:

$$\delta V = \frac{d}{\Delta t^2}\frac{2}{Fe}$$

where $d$ is the distance between the wires. The relative uncertainty is equal to:

$$\frac{\delta V}{V} = \pm\frac{V}{d}\frac{2}{Fe}$$

For each flow condition, the acquisition frequency is shown in Table 1. These values guarantee that the relative uncertainty of the bubble velocity is always smaller than 0.5%.

Table 1
Acquisition frequency

| | | | | | | | | |
|---|---|---|---|---|---|---|---|---|
| Liquid velocity (m/s) | 0.5 | 0.6 | 0.7 | 0.8 | 1.0 | 1.2 | 1.5 | 1.8 |
| Bubble velocity (m/s) | 0.80 | 0.90 | 1.00 | 1.11 | 1.32 | 1.53 | 1.85 | 2.20 |
| Frequency (Hz) | 300 | 350 | 400 | 450 | 550 | 600 | 750 | 900 |

## 3. Experimental results

For each run, a single bubble is injected in the pipe at a constant liquid flow rate. The test campaign covered a wide range of liquid flow velocity. For each flow rate, bubbles with different volumes were observed. Each bubble was detected by five wire probes and one ring probe. The good agreement of measured data from these different sensors, shown in Fig. 5, ensures that the assumption of a horizontal liquid–gas interface was correct. The figure also shows that the ring probe is not able to detect the wavy interface owing to its weak spatial resolution, contrary to the wires.

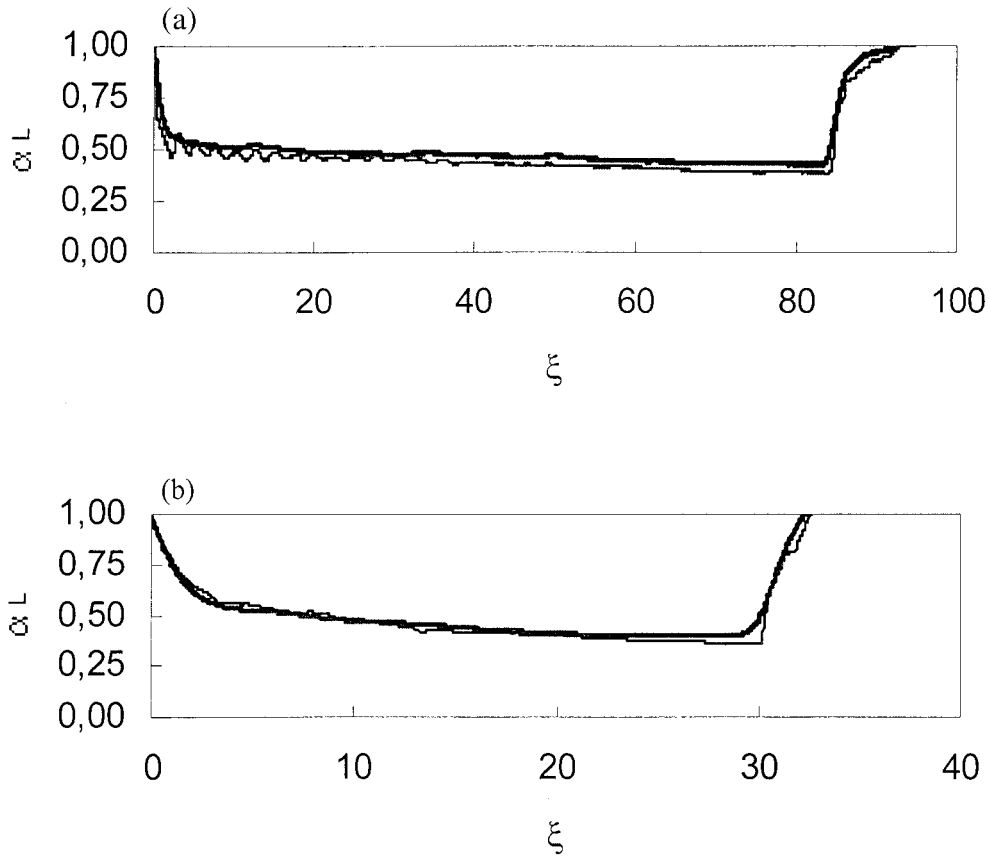


Fig. 5. Comparison between wire and ring sensor: (a) 0.7 m/s, (b) 1.5 m/s. ——— Wire; ——— Ring.

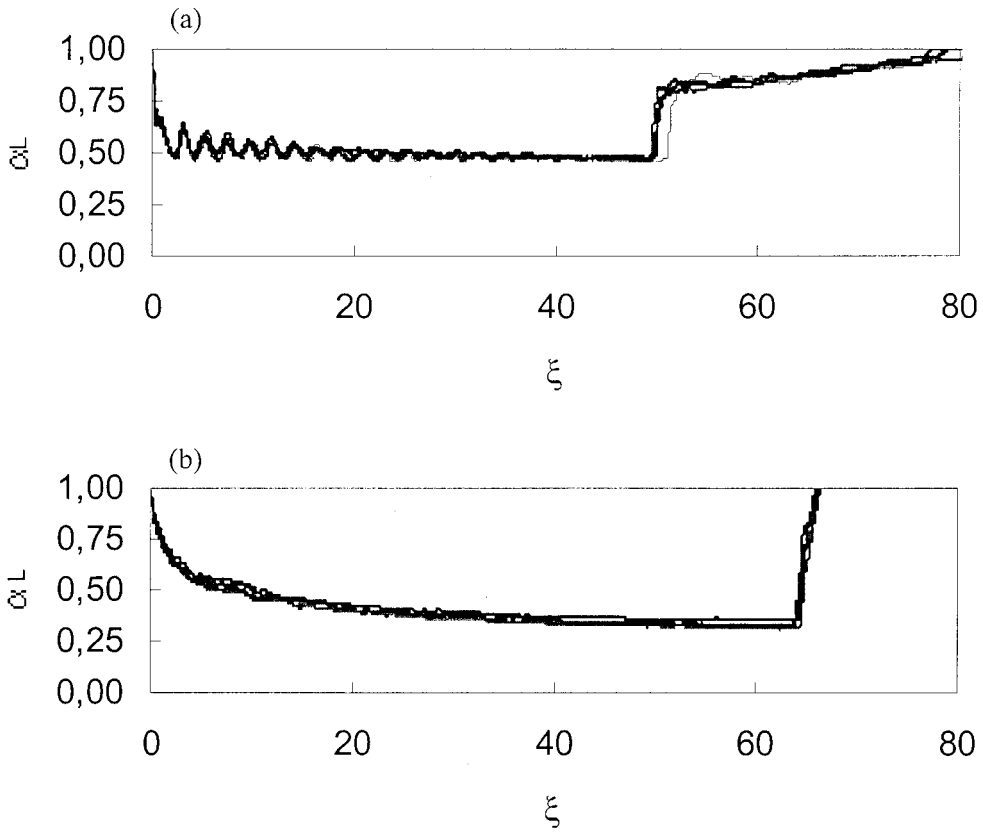


Fig. 6. Superposition of the signal from five wires: (a) 0.5 m/s, (b) 1.8 m/s.

Fig. 6 shows the superposition of data from the five wires for a single bubble, at two different velocities. The agreement of the five curves shows that the bubble shape remains fairly unchanged during its motion. The figure also shows that two categories of bubbles may be distinguished, according to their shape. The transition was observed to be mainly function of the liquid velocity $U$ ahead of the bubble. From dimensional analysis, it reduces to a function of the Froude number defined by:

$$Fr_U = \frac{U}{\sqrt{gD}}$$

where $g$ is the gravity and $D$ the pipe diameter.

At low velocities, typically when the Froude number is smaller than 1, Fig. 6a shows that the bubble presents a short nose followed by a wavy interface with a constant wavelength and a decreasing amplitude. It ends with a level jump that can be viewed as a hydraulic jump attached to the bubble end. This hydraulic jump does not reach the top of the pipe. It creates a tail behind the bubble that gives a staircase aspect. It is interesting to note that the wavy interface observed at low flow rates is frozen, indicating that it is stationary in the frame moving with the bubble.

As the Froude number increases, the nose becomes longer, the wave amplitude smaller and the tail thinner and shorter. For single bubbles, the tail is always attached to the bubble. Nevertheless, Grenier (1997) observed that in regular slug flows, the tail may detach from time to time from the bubble. The reason is that in slug flow, the velocity of each bubble oscillates, as successive bubbles and liquid slugs leave the pipe. This oscillation causes the level jump at the back of the bubble to vary and, if it reaches the top of the pipe, the tail separation occurs.

For high velocities, typically when $Fr_U$ is greater than 2, the tail and the stationary wave attached to the nose disappear, as shown in Fig. 6b. In the absence of tail, it was observed that small bubbles are entrained in the wake of the long bubble. Fig. 7 shows pictures from the bubble tail at different velocities. It confirms that the slug behind the bubble is free of bubbles when the tail is present (pictures 'a' and 'b') in contrast to picture 'c', where the level jump reaches the top of the pipe and the entrainment of small bubbles is observed.

The theoretical transition between the shape of two bubbles is proposed in Section 4. Ruder and Hanratty (1990) used this shape characteristic to define the transition between the plug flow and the slug flow regimes.

The position of the bubble nose is not detected by the wire probes. They measure the total height of the wire wetted by the liquid and it is assumed that the liquid occupies the lower section. Fig. 8 shows that this assumption is valid for small velocities. The nose is located on the top of the pipe and its tip touches the upper wall. At higher velocities, however, Fig. 8c shows that the nose of the bubble moves toward the centre of the pipe, as observed by Bendiksen (1984).

For a fixed liquid flow rate, bubbles with different volumes lie on a same basic shape, as

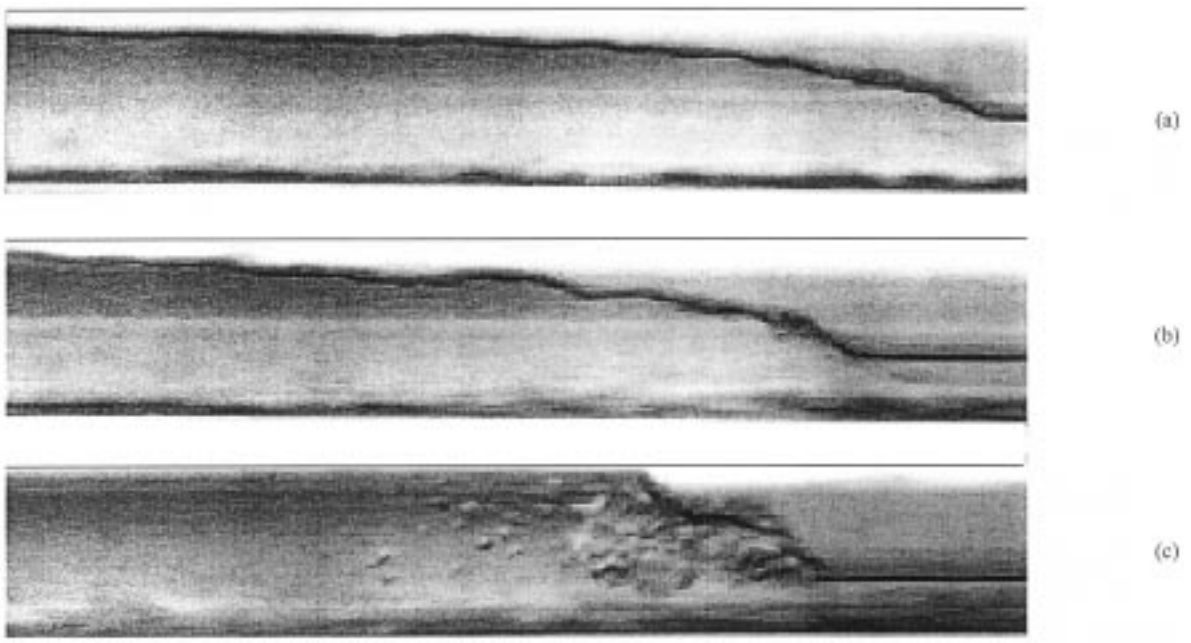


Fig. 7. Bubble tail: (a) 0.6 m/s, (b) 1.0 m/s, (c) 1.5 m/s.

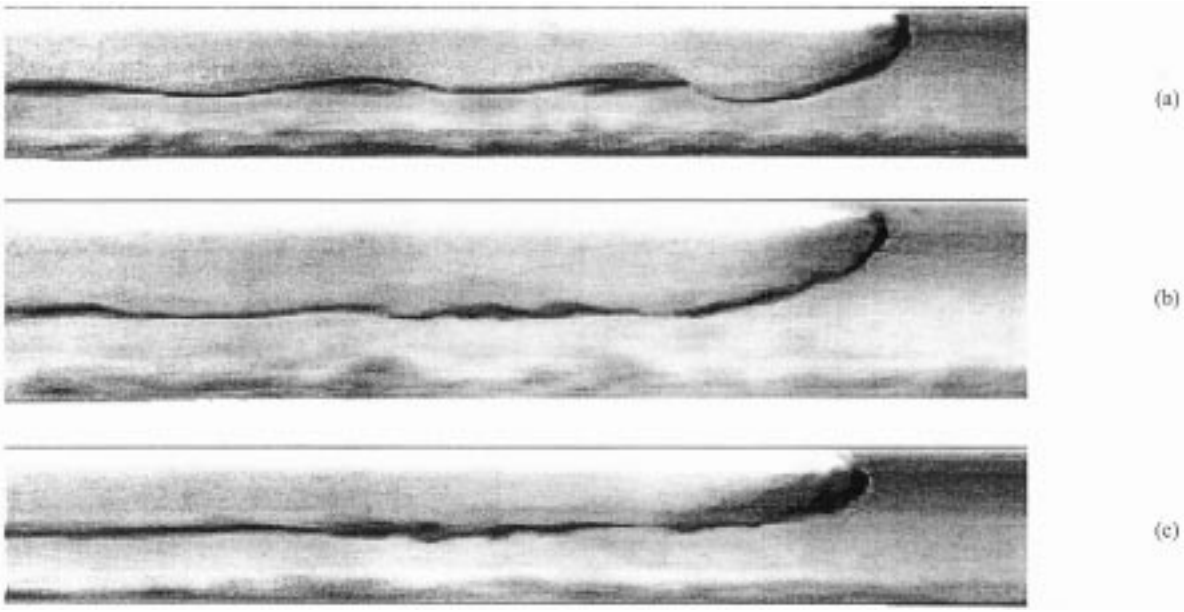


Fig. 8. Bubble nose: (a) 0.6 m/s, (b) 1.0 m/s, (c) 1.5 m/s.

shown in Fig. 9. This agrees with the conclusion of Grenier et al. (1997). Fig. 9a shows that the stationary wave attached to the bubble nose is independent of the bubble length. It also shows that the shorter the bubble, the longer the tail. It will be seen that shorter bubbles have thicker film, which means faster liquid film: the intensity of the hydraulic jump behind the bubble is smaller and thus it creates longer tails.

## 4. Bubble shape model

The present analysis is limited to horizontal flow. The bubble is divided in four regions, as defined in Fig. 10: the nose, the body, the hydraulic jump at the back and the tail, if it exists. The back end of the slug that precedes the bubble is assumed non-aerated, as well as the liquid film.

### 4.1. Bubble body

The solution for the bubble body is similar to the bubble shape model described by Andreussi et al. (1993). It is based on the mass and momentum conservation of each phase:

$$\frac{\partial \alpha_K}{\partial t} + \frac{\partial (\alpha_K u_K)}{\partial x} = 0$$

$$\frac{\partial (\alpha_K u_K)}{\partial t} + \frac{\partial \left(\alpha_K u_K^2\right)}{\partial x} + \frac{\alpha_K}{\rho_K}\frac{\partial p_{\mathrm{i}}}{\partial x} + \alpha_K g \frac{\partial H}{\partial x} = \frac{\tau_K^{\mathrm{W}} S_K + \tau_K^{\mathrm{i}} S_{\mathrm{I}}}{\rho_K A}$$

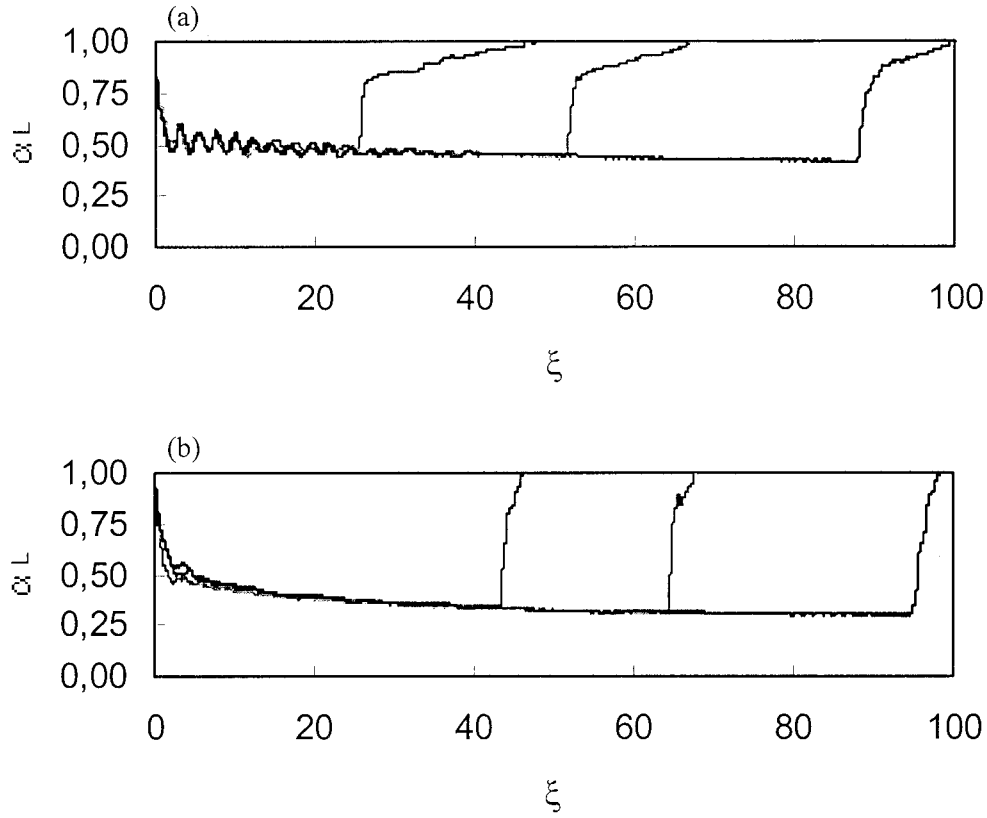


Fig. 9. Influence of the bubble volume: (a) 0.6 m/s, (b) 1.2 m/s.

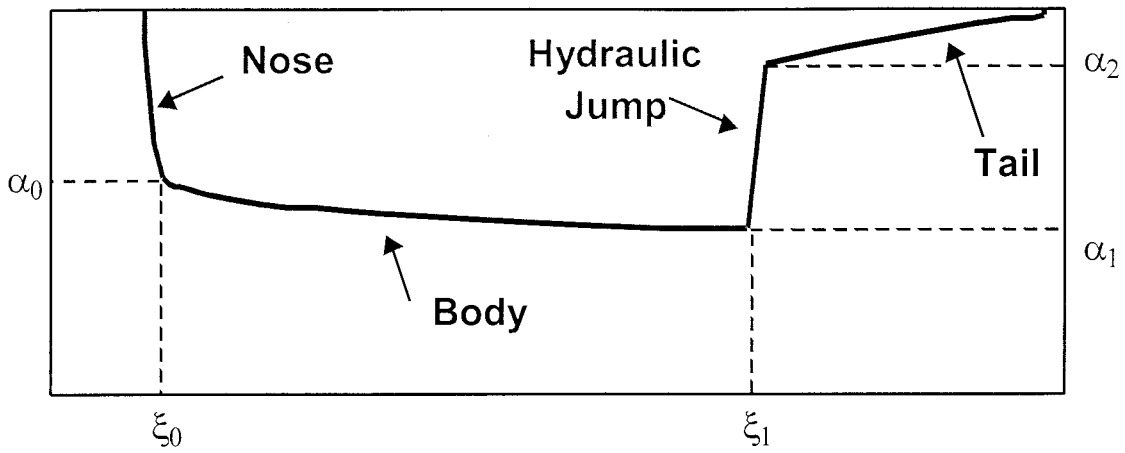


Fig. 10. Bubble regions.

where $\alpha_K$,$\rho_K$ and $u_K$ are, respectively, the volume fraction, the density and the velocity of phase $K$, $p_i$ the interfacial pressure, $A$, the tube cross-section and $H$, the vertical position of the interface. The shear stresses exerted by the wall and by the interface upon the phase $K$ are $\tau_K^W$ and $\tau_K^i$, respectively. $S_K$ is the wall perimeter wetted by phase $K$ and $S_I$ is the interfacial perimeter. As it stands, the momentum equation is written in the frame of long wave approximation. Some tricky simplifications allow a simple analytical solution of these differential equations.

We will use a new set of variables: $\xi = (Vt - x)/D$ and $\tau = t$, where $V$ is the bubble nose velocity and $\xi$ is the distance from the bubble nose divided by the pipe diameter. Considering that the shape does not change in time, and eliminating the pressure term, the partial differential equations reduce to:

$$\alpha_L(V - u_L) = \varphi \tag{1}$$

$$\alpha_G(V - u_G) = 0 \tag{2}$$

$$\frac{\varphi^2}{\alpha_L^3}\frac{d\alpha_L}{d\xi} - g'D\frac{dh}{d\xi} = \frac{4}{\rho_L}\left(\frac{\tau_L^W s_L}{\alpha_L} - \frac{\tau_G^W s_G}{\alpha_G} - \frac{\tau_G^i s_I}{\alpha_G \alpha_L}\right) \tag{3}$$

where $\varphi$ is the liquid flux under the bubble. The dimensionless parameter $s_K = S_K/S$ was introduced, $S$ being the pipe perimeter. For a non-aerated liquid slug, $\varphi = V - U$, $U$ being the mean liquid velocity ahead of the bubble. The modified gravitational acceleration is $g' = g\Delta\rho/\rho_L$ and $h = H/D$.

Far enough from the nose ($\xi \to \infty$), the flow in the liquid film is fully developed. The LHS of Eq. (3) vanishes and the solution $\alpha_{L\infty}$ is given from:

$$\alpha_{L\infty}(V - u_{L\infty}) = \varphi \tag{4}$$

$$\alpha_{G\infty}(V - u_{G\infty}) = 0 \Longrightarrow V = u_{G\infty} \tag{5}$$

$$\frac{\tau_{L\infty}^W s_{L\infty}}{\alpha_{L\infty}} - \frac{\tau_{G\infty}^W s_{G\infty}}{\alpha_{G\infty}} - \frac{\tau_{G\infty}^i s_{I\infty}}{\alpha_{G\infty}\alpha_{L\infty}} = 0 \tag{6}$$

The volume fraction of the liquid film far from the nose can be determined if closure laws are known for the wall and interfacial shear stresses. Assuming that the liquid film velocity $u_{L\infty}$ is much smaller than the bubble velocity $V$, as proved further:

$$\tau_L^W = -\frac{1}{2}\rho_L f_L u_L^2$$

$$\tau_G^W = -\frac{1}{2}\rho_G f_G V^2$$

$$\tau_G^i = -\frac{1}{2}\rho_G f_I (V - u_L)^2 \cong -\frac{1}{2}\rho_G f_I V^2 \tag{7}$$

where $f$ is the friction factor. Assuming that both gas and liquid flows are in a turbulent regime, the friction factors are expressed by:

$$f_L = C(Re_L)^{-n}, \quad Re_L = \frac{u_\infty D}{\nu_L}\left(\frac{\alpha_L}{s_L}\right)$$

$$f_I \cong f_G = C(Re_G)^{-n}, \quad Re_G = \frac{VD}{\nu_G}\left(\frac{\alpha_G}{s_G + s_I}\right) \tag{8}$$

Substituting Eqs. (7) and (8) in Eq. (6), a relation between the liquid velocity and the liquid fraction far from the nose appears:

$$u_{L\infty}^2 = \left(\frac{\alpha_{L\infty} s_{G\infty} + s_{I\infty}}{\alpha_{G\infty} s_{L\infty}}\right)\frac{\rho_G}{\rho_L}\left(\frac{Re_L}{Re_G}\right)^n V^2$$

It is possible to separate the influence of fluid properties and phase fraction in writing the above equation under the form:

$$u_{L\infty} = \beta \Phi V \tag{9}$$

Assuming for $f$, the validity of Blasius relationship, $n$ equals 1/4. It yields:

$$\beta = \left(\frac{\nu_G \rho_G^4}{\nu_L \rho_L^4}\right)^{1/7} \quad \text{and} \quad \Phi = \left[\frac{(\alpha_{L\infty} s_{G\infty} + s_{I\infty})^4 \alpha_{L\infty}(s_{G\infty} + s_{I\infty})}{(\alpha_{G\infty} s_{L\infty})^5}\right]^{1/7}$$

where $\Phi$ is a function of the liquid fraction and $\beta$ depends only on the fluids properties. For air and water at atmospheric pressure, $\beta = 0.0315$. Combining Eqs. (9) and (4) leads to

$$\alpha_{L\infty}\left[1 - \beta\Phi(\alpha_{L\infty})\right] = \frac{\varphi}{V} \tag{10}$$

The above implicit equation in $\alpha_{L\infty}$ can be solved by noting that $\beta$ is a small parameter. Thus $\alpha_{L\infty}$ can be expressed through an asymptotic series:

$$\alpha_{L\infty} = \alpha_{L0} + \beta\alpha_{L1} + \beta^2\alpha_{L2} + \cdots \tag{11}$$

The next step is to introduce Eq. (11) into (10) and to separate the terms by powers of $\beta$. The first and second terms give the values of $\alpha_{L0}$ and $\alpha_{L1}$:

$$\beta^0 \Longrightarrow \alpha_{L0} = \frac{\varphi}{V}$$

$$\beta^1 \Longrightarrow \alpha_{L1} = \alpha_{L0}\Phi(\alpha_{L0})$$

and the solution to the liquid fraction far from the nose is given by:

$$\alpha_{L\infty} = \frac{\varphi}{V}\left[1 + \beta\Phi\left(\frac{\varphi}{V}\right)\right] \tag{12}$$

As far as the liquid fraction far from the nose falls between 0.1 and 0.5, Appendix A shows that the function $\Phi$ may be replaced by a linear relation:

$$\Phi(\alpha_L) = 1.70(\alpha_L + 0.5) \tag{13}$$

The general solution is obtained replacing Eq. (13) into (12):

$$\alpha_{L\infty} = \frac{\varphi}{V}\left[1 + 1.70\left(\frac{\varphi}{V} + 0.5\right)\left(\frac{\nu_G\rho_G^4}{\nu_L\rho_L^4}\right)^{1/7}\right] \tag{14}$$

In the particular case of water and air at atmospheric pressure, Eq. (14) simplifies to:

$$\alpha_{L\infty} = 1.027\frac{\varphi}{V} + 0.054\left(\frac{\varphi}{V}\right)^2 \tag{15}$$

Combining Eq. (15) and the mass conservation equation (4), a relation between the film velocity far from the nose $u_{L\infty}$ and the known parameters $V$ and $\varphi$ is deduced:

$$u_{L\infty} = \frac{0.027 + 0.054\varphi/V}{1.027 + 0.054\varphi/V}V \tag{16}$$

The ratio $\varphi/V$ is typically between 0.15 and 0.50. In this range, the film velocity far from the nose $u_{L\infty}$ varies from 0.034 to 0.051 V. This justifies the previous assumption that the liquid velocity in the film is small in comparison to the bubble velocity.

The momentum equation (3) may be rewritten to introduce the shear stress upon the liquid, far from the nose:

$$\frac{\varphi^2}{\alpha_L^3}\frac{d\alpha_L}{d\xi} - g'D\frac{dh}{d\xi} = \frac{4}{\rho_L}\left(\frac{\tau_L^W s_L}{\alpha_L} - \frac{\tau_G^W s_G}{\alpha_G} - \frac{\tau_G^i s_I}{\alpha_G\alpha_L}\right)$$

$$-\frac{4}{\rho_L}\left(\frac{\tau_{L\infty}^W s_{L\infty}}{\alpha_{L\infty}} - \frac{\tau_{G\infty}^W S_{G\infty}}{\alpha_{G\infty}} - \frac{\tau_{G\infty}^i s_{G\infty}}{\alpha_{G\infty}\alpha_{L\infty}}\right) \tag{17}$$

Re-arranging the terms we may write

$$\frac{\varphi^2}{\alpha_L^3}\frac{d\alpha_L}{d\xi} - g'D\frac{dh}{d\xi} = \frac{4}{\rho_L}\left(\frac{\tau_L^W s_L}{\alpha_L} - \frac{\tau_{L\infty}^W s_{L\infty}}{\alpha_{L\infty}}\right) - \frac{4}{\rho_L}\left(\frac{\tau_G^W s_G}{\alpha_G} + \frac{\tau_G^i s_I}{\alpha_G\alpha_L} - \frac{\tau_{G\infty}^W s_{G\infty}}{\alpha_{G\infty}} - \frac{\tau_{G\infty}^i s_{I\infty}}{\alpha_{G\infty}\alpha_{L\infty}}\right) \tag{18}$$

The second term on the RHS is small in comparison to the first term. As a matter of fact, the ratio between the two terms is proportional to the ratio between the gas and the liquid densities, which is about 1:1000 for air and water. Eq. (18) may be simplified to:

$$\frac{\varphi^2}{\alpha_L^3}\frac{d\alpha_L}{d\xi} - g'D\frac{dh}{d\xi} = \frac{4}{\rho_L}\left(\frac{\tau_L^W s_L}{\alpha_L} - \frac{\tau_{L\infty}^W s_{L\infty}}{\alpha_{L\infty}}\right) \tag{19}$$

Assuming that $f_L = f_{L\infty}$, the equation above may be re-written in terms of the liquid fraction far from the nose (Fagundes Netto, 1999):

$$\frac{\varphi^2}{\alpha_L^3}\frac{d\alpha_L}{d\xi} - g'D\frac{dh}{d\xi} = -2f_L\frac{s_L}{\alpha_L^3}\left(\frac{\alpha_L - \alpha_{L\infty}}{\alpha_{L\infty}}\right)^2\varphi^2 \tag{20}$$

Eq. (20) will be used with $\alpha_{L\infty}$ given by Eq. (14) or (15). The body shape is then described by:

$$\frac{\left(1 - k\alpha_L^3\right)}{s_L(\alpha_L - \alpha_{L\infty})^2}\,d\alpha_L = -\frac{2f_L}{(\alpha_{L\infty})^2}\,d\xi \tag{21}$$

where

$$k = \frac{dh}{d\alpha_L}\frac{g'D}{\varphi^2} = \frac{1}{4s_I}\frac{g'D}{\varphi^2}$$

It must be pointed out that $s_L$ and $dh/d\alpha_L$ are functions of $\alpha_L$. The solution $\alpha_L(\xi)$ of Eq. (21) possesses two branches according to the sign of $(1 - k\alpha_L^3)$. Returning to dimensional parameters and taking into account that $dh/d\alpha_L = 1/(4s_I)$, this term can be written under the form:

$$1 - k\alpha_L^3 = 1 - Fr_F^2$$

where $Fr_F = (V - u_L)/\sqrt{g'H_M}$ is the film Froude number in which $H_M = A\alpha_L/S_I$ is the mean liquid height.

A typical solution of Eq. (21) is shown in Fig. 11. The upper branch corresponds to $1 - k\alpha_L^3 < 0$, i.e., $Fr_F > 1$. The lower branch corresponds to $1 - k\alpha_L^3 > 0$, i.e., $Fr_F < 1$. For the bubble body, we are looking for solutions where $d\alpha_L/d\xi$ is negative, corresponding to the lower branch. For this branch, $\alpha_L$ is always smaller than $k^{-1/3}$. Moreover, it is also greater than its asymptotic value far from the nose. Therefore, the body solution is valid only when $\alpha_{L\infty} < \alpha_L < k^{-1/3}$.

As it stands, Eq. (21) has no analytical solution. An approximated solution can be found for $\alpha_L$ in the range [ 0.2, 0.8 ]. In this case, it is found (see Appendix A) that:

$$\frac{dh}{d\alpha_L} \cong 0.820 \quad \text{and} \quad s_L \cong \frac{\alpha_L + 0.5}{2}$$

Considering the friction factor constant and equal to its value at the liquid slug ($f_{L0}$), Eq. (21) becomes

$$\frac{\left(1 - k\alpha_L^3\right)d\alpha_L}{(\alpha_L + 0.5)(\alpha_L - \alpha_{L\infty})^2} = -\frac{f_{L0}}{(\alpha_{L\infty})^2}d\xi \tag{22}$$

where $k = 0.820g'D/\varphi^2$ Eq. (22) may be integrated analytically and its solution is

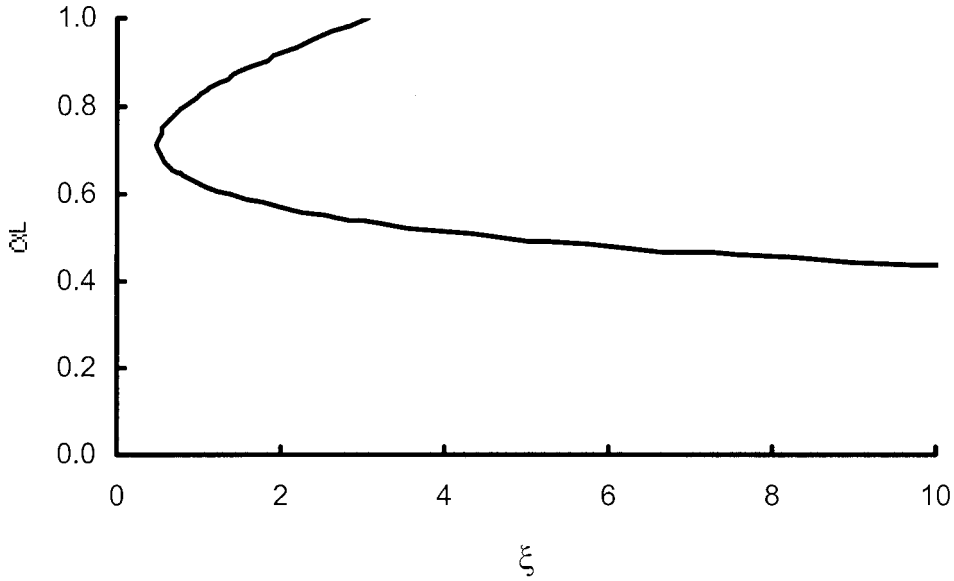


Fig. 11. Bubble shape: body solution for $U = 1.8$ m/s and $V = 2.2$ m/s.

$$-\left(1+\frac{k}{8}\right)\ln\left(\frac{2\alpha_L+1}{2\alpha_{L0}+1}\right)+\left(1+k\alpha_{L\infty}^2(1.5+2\alpha_{L\infty})\right)\ln\left(\frac{\alpha_L-\alpha_{L\infty}}{\alpha_{L0}-\alpha_{L\infty}}\right)$$

$$-(\alpha_{L\infty}+0.5)^2\left\{\frac{(1-k\alpha_{L\infty}^3)}{(\alpha_{L\infty}+0.5)(\alpha_{L0}-\alpha_{L\infty})(\alpha_L-\alpha_{L\infty})}-k\right\}(\alpha_L-\alpha_{L0})$$

$$=f_{L0}\left(\frac{\alpha_{L\infty}+0.5}{\alpha_{L\infty}}\right)^2(\xi-\xi_0) \tag{23}$$

where the initial condition $(\xi_0,\alpha_{L0})$ will be given by the nose model.

### 4.2. Bubble nose

Eqs. (1)–(3) cannot describe the nose of the bubble because in this region $dh/d\alpha_L$ is not weak and the long wave approximation fails. Moreover, it was seen that at high velocities, the nose moves toward the centre of the pipe. In this situation, the liquid velocity around the nose is necessarily 3D, and a 2D model cannot predict its actual shape. As a sophisticated 3D model, for the bubble nose is out of the scope of this paper and considering that the nose length is less than one pipe diameter, the solution proposed by Benjamin (1968) for pipe voidage and developed in the frame of the inviscid theory was used. This solution is given, after correction

of a typographic error, by:

$$\xi = \frac{1}{4\pi(a^2 - 2ab + 4b^2)}\left\{3a(2-a)\ln\left(\frac{a^2 + 2abR + 4b^2R^2}{a^2}\right)\right.$$

$$+3\left(2b^2 - ab + a\right)\ln\left(1 - R + R^2\right) + 2\left(2a^2 - ab + 2b^2 - 3a\right)\ln\left(1 + R^3\right)$$

$$\left.+2\sqrt{3}\left(2b^2 + ab + a - 4b\right)\left[\sin^{-1}\left(\frac{\sqrt{3}/2}{\sqrt{1 - R + R^2}}\right) - \frac{\pi}{3}\right]\right\}$$

$$h = 1 + \frac{1}{4\pi(a^2 - 2ab + 4b^2)}\left\{6a(2-a)\tan^{-1}\left(\frac{\sqrt{3}bR}{a + bR}\right) + 6\left(2b^2 - ab + a\right)\tan^{-1}\left(\frac{\sqrt{3}R}{R-2}\right)\right.$$

$$\left.+\sqrt{3}\left(2b^2 + ab + a - 4b\right)\ln\left(\frac{(1+R)^2}{1 - R + R^2}\right)\right\}$$

where $a = 1.49$, $b = 0.85$ and $R$ is positive. We are looking for solutions with $\xi<1$. In this range the Benjamin solution may be approximated by a second-order polynomial equation:

$$\alpha_L = 1 - 0.775\xi + 0.345\xi^2 \tag{24}$$

The nose solution of the bubble shall fit the body solution at $(\xi_0,\alpha_{L0})$, where both curves have the same inclination:

$$-\frac{d\alpha_L}{d\xi}|_{\alpha_{L0}} = \frac{f_{L0}(\alpha_{L0} + 0.5)}{1 - k\alpha_{L0}^3}\left(\frac{\alpha_{L0} - \alpha_{L\infty}}{\alpha_{L\infty}}\right)^2 = \sqrt{1.38(\alpha_{L0} - 0.5648)} \tag{25}$$

As the nose region is arbitrarily defined as $\xi \le 1$, $\alpha_{L0}$ must fall within $[\alpha_{LM},1]$ where $\alpha_{LM} = 0.57$ from Eq. (24) and $\xi = 1$. Moreover, $\alpha_{L0}$ must also belong to the body solution that falls within $[\alpha_{L\infty},k^{-1/3}]$. Combining these conditions leads to:

$$\alpha_{LM}<\alpha_{L0}<k^{-1/3}$$

With $\alpha_{L0}$ given numerically by Eq. (25), $\xi_0$ is determined by (24). When $\xi<\xi_0$, the nose Eq. (24) is applied. Otherwise, Eq. (23) is applied with initial condition $(\xi_0,\alpha_{L0})$.

### 4.3. Hydraulic jump

The next step is to evaluate the jump intensity at the back of the bubble (Fig. 12). Following Wallis (1969), the equation through the singularity may be obtained using the mass and momentum balance equations across it. If the pressure in the gas phase is supposed constant, the momentum balance is:

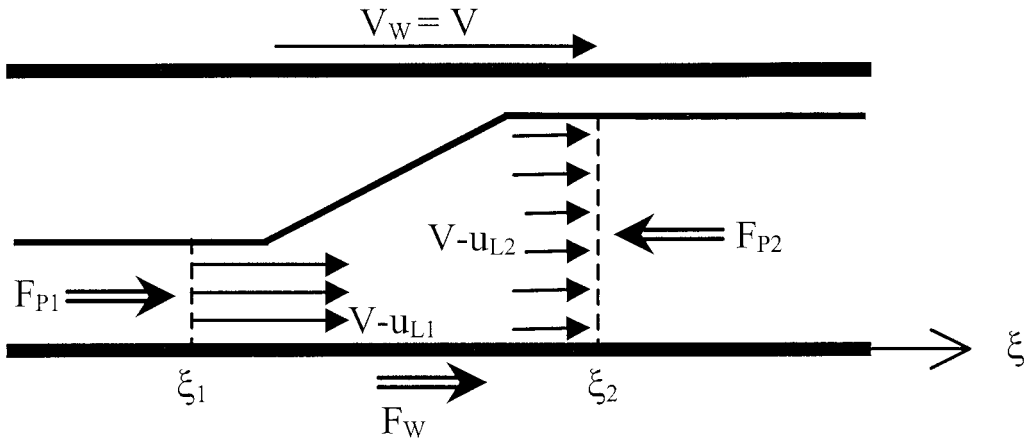


Fig. 12. Hydraulic jump at the back of the bubble.

$$(\text{Momentum out}) - (\text{Momentum in}) = F_{P1} - F_{P2} + F_W$$

which leads to:

$$\rho_L \rho_{L1}(V-u_{L1})^2 + \rho_L g \int_0^{\alpha_{L1}} (H_1 - z)\, d\alpha_L = \rho_L \alpha_{L2}(V-u_{L2})^2 + \rho_L g \int_0^{\alpha_{L2}} (H_2 - z)\, d\alpha_L - \frac{F_W}{A}$$

where $F_W$ is the force exerted by the pipe wall upon the liquid, across the jump. In the $\xi$-frame, the wall velocity is greater than the liquid velocity. Thus the force exerted by the wall upon the liquid is a driving force ($F_W > 0$) and not a resisting force as suggested by Ruder and Hanratty (1990).

If we define $f(\alpha_L) = \int_0^{\alpha_L} (H - z)/D\, d\alpha_L$:

$$\frac{Fr_R^2}{\alpha_{L1}} + f(\alpha_{L1}) = \frac{Fr_R^2}{\alpha_{L2}} + f(\alpha_{L2}) - \frac{F_W}{\rho_L g D A} \tag{26}$$

where $Fr_R = \varphi/\sqrt{gD}$ is the Froude number based on the relative velocity.

At a fixed $Fr_R$, for each value of $\alpha_{L1}$ there is only one value of $\alpha_{L2}$ satisfying Eq. (26). If $\alpha_{L2} \geq 1$, the hydraulic jump reaches the top of the pipe and there is no tail at the back of the bubble.

Before studying the transition between plug and slug regimes, we shall recall the usual closure laws concerning the bubble velocity as a function of the mixture velocity. From the study of Bendiksen (1984), it is generally accepted that the bubble velocity may be determined by

$$V = C_0 U + C_\infty \sqrt{gD}$$

where $C_0$ and $C_\infty$ are coefficients that depend on the mixture Froude number $Fr_U$. For $Fr_U > 3.5$, Bendiksen proposed that $C_0 = 1.2$ and the drift coefficient $C_\infty$ vanishes. For $Fr_U < 3.5$, $C_0$ is usually taken equal to 1 and the drift coefficient is positive. Benjamin (1968)

showed that for inviscid flow this coefficient equals 0.54. Weber (1981) proposed a correction of this value given by:

$$C_\infty = 0.542 - \frac{1.76}{Bo^{0.56}}$$

where the Bond number, $Bo$, depends on the superficial tension $\sigma$ and is defined by:

$$Bo = \frac{\Delta\rho g D^2}{\sigma}$$

For air and water in a 53 mm pipe, $Bo \cong 390$ and the drift coefficient equals 0.48. To keep the function between $V$ and $U$ continuous, the critical Froude number should be taken equal to:

$$Fr_{\text{crit}} = \frac{C_\infty}{0.2}$$

As a consequence, for $Fr_U < Fr_{\text{crit}}$, the relative velocity Froude number, $Fr_R$, is constant and equal to the drift coefficient $C_\infty$. On the contrary, when $Fr_U > Fr_{\text{crit}}$, it may be written that $Fr_R = 0.2Fr_U$. For the present case, it must be pointed out that $Fr_{\text{crit}}$ is equal to 2.4.

Experience shows that the hydraulic jump is not vertical, but along a finite length $L_J = \xi_2 - \xi_1$ (see Fig. 12) as it moves with the bubble. The pipe wall exerts a force upon the liquid between points 1 and 2 given by:

$$F_W = \int_{\xi_1}^{\xi_2} \tau_L^W S_L \, d\xi$$

The shear stress $\tau_L^W$ may not be estimated by usual steady-state closure laws because the flow between positions 1 and 2 is disturbed by the wake. The liquid velocity profile in this region suggests that the shear stress is much higher than the shear stress estimated, considering fully developed flow. It is reasonable to consider that the shear stress in this region is somehow proportional to the shear stress in the slug, $\tau_{L0}^W$:

$$F_W = L_J \langle S_L \tau_L^W \rangle_{\text{JUMP}} = C_J L_J S \tau_{L0}^W \quad \text{where} \quad C_J = \frac{\langle S_L \tau_L^W \rangle_{\text{JUMP}}}{S \tau_{L0}^W} \tag{27}$$

The coefficient $C_J$ and the jump length $L_J$ were determined experimentally. The jump length varied between 0.7 and $1.3D$ and it was assumed that $L_J \cong 1D$. The best fit to data was achieved with $C_J = 4$. Ruder and Hanratty (1990) used a similar expression with $C_J$ equal to unity and $L_J$ in the range between 2 and $8D$, that does not correspond to observed lengths of the hydraulic jump.

Fig. 13 shows how the transition between plug and slug regimes, defined by the existence or not of a tail at the back of the bubble (Ruder and Hanratty, 1990), may be determined. The figure presents the liquid volume fraction $\alpha_{L1}$ before the hydraulic jump as a function of the mixture Froude number ($Fr_U$). Two set of curves are plotted: the solid curve gives the value of $\alpha_{L1}$ when the jump reaches the top of the pipe. It is determined by Eq. (26) with $\alpha_{L2} = 1$, the force $F_W$ exerted by the wall being neglected. Note that as $\varphi$ does not depend on the liquid

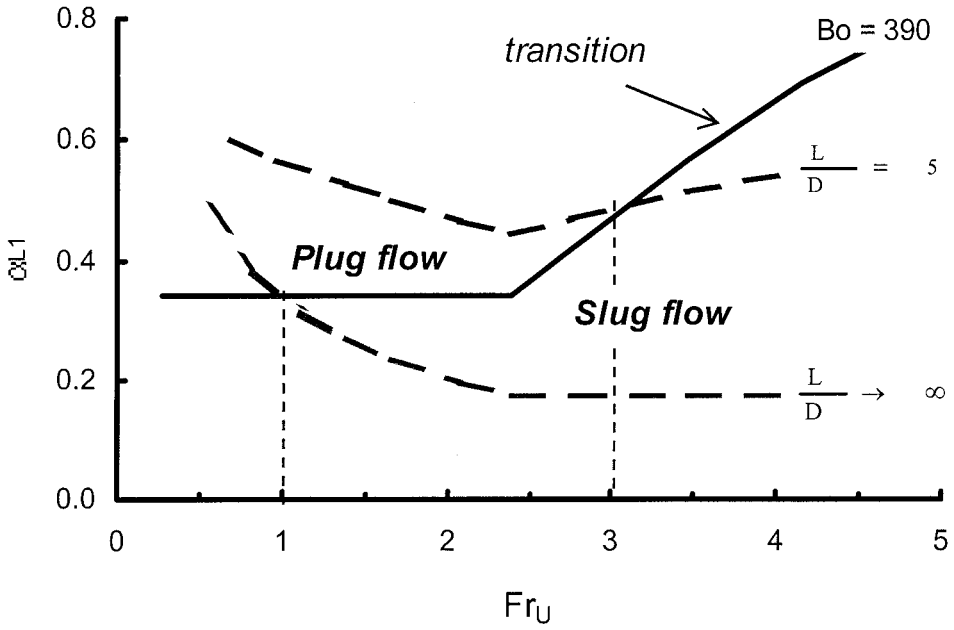


Fig. 13. Transition between the two intermittent regimes.

velocity for small values of the Froude number, the transition is represented in this region by a horizontal line. Bubbles with value of $\alpha_{L1}$ that fall above this curve have a staircase shape, corresponding to plug flow. The dashed curves correspond to bubbles with a given length, determined numerically from Eq. (23). The figure shows that for $Fr_U$ smaller than 1, staircase bubbles are always observed. In contrast, when $Fr_U$ is greater than 3, every bubble longer than $5D$ is in the slug regime. At intermediate values of $Fr_U$, between 1 and 3, the existence of the tail depends on the bubble length.

From experiments carried out in 95.3 mm pipe, Ruder and Hanratty (1990) suggested that the transition between plug and slug flow regimes is independent of the superficial liquid velocity and occurs at a fixed gas velocity of about 0.6 m/s. It must be pointed out in passing, that their experimental study is based on observation using a wide range of gas velocity (0.018–0.62 m/s) and a rather narrow range of liquid velocity (0.50–0.95 m/s). In the present study, the model suggests that there exists for some mixture velocities, a transition region in which it should be observed short bubbles with tail and longer bubbles without it. If a transition has to be defined precisely in this region, it must be based on the shape of the bubble whose length is equal to the average. At a given mixture flow rate, there is only one value of $\alpha_{L1}$ that balances Eq. (26) with $\alpha_{L2} = 1$. This liquid fraction ($\alpha_{L1}$) gives the bubble length at transition. Assuming that the mean slug length $L_S$ is known, one can easily determine the liquid and gas superficial velocities that represent the transition line. Fig. 14 shows the transition line for water and air flowing in a pipe of 95.3 mm, the same diameter used by Ruder and Hanratty. (A) and (B) are constant mixture velocity lines that limit the transition region. When the mixture velocity is smaller than the value given by (A), the staircase shape is always observed. When it is higher than (B), it is never observed. Between these values, the

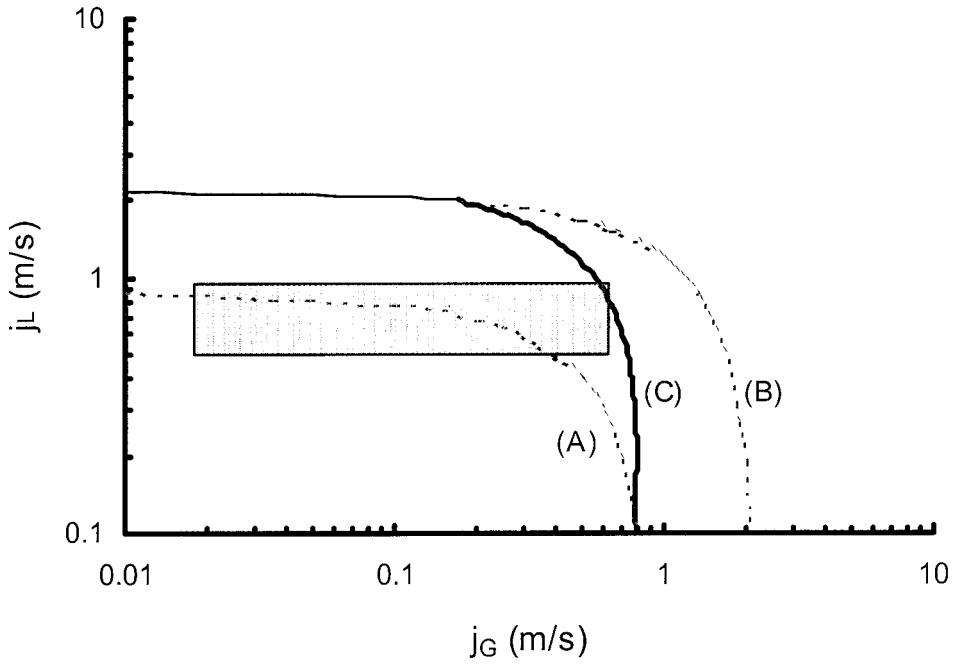


Fig. 14. Regime transition, $D = 95.3$ mm, $L_S = 32D$.

transition line (C) depends on the bubble length. The rectangle, representing the experiments reported by Ruder and Hanratty, shows that their observation is not contradictory with the transition determined in this study from the shape of isolated bubbles.

### 4.4. Bubble tail

When a tail exists, its shape corresponds to the upper branch of Fig. 11. In this case, Eq. (21) is solved with $k\alpha_L^3 > 1$. As the tail is usually confined at the very top of the pipe, we may consider $\alpha_L \to 1$ and linearise Eq. (3) assuming $s_L \to 1$ and $d\alpha_L/dh \to 0$.

The equation for the tail simplifies to a linear relation between $h$ and $\xi$:

$$\frac{dh}{d\xi} = 2f_{L0}\frac{U^2}{g'D} = \text{constant} \tag{28}$$

### 4.5. Flow regime in the liquid film

In the present case, the Reynolds number $Re_\infty = u_{L\infty}(\alpha_{L\infty}/s_{L\infty})D/\nu_L$ of the liquid film far from the nose is always greater than 2500. With this value the flow is close to the transition expected for fully developed flow, although this transition is not well known for free surface flow in circular pipe. However, the flow regime ahead of the bubble nose is clearly turbulent since the Reynolds number is always greater than 25,000. For the flow in the liquid film to become laminar, the turbulence created ahead of the bubble must be killed during the residence

time of the liquid in the film. For $80D$ bubbles in liquid velocity of 0.5 m/s, this time is about 5 s. It is likely that the laminarisation does not occur in such a short time.

## 5. Model validation

The model requires four input parameters: the pipe internal diameter, the liquid flow velocity, the bubble velocity and its volume. To solve the bubble shape, the value of $\alpha_{L\infty}$ is initially determined by Eq. (14) or (15). The value of $\alpha_{L0}$ is then determined by Eq. (25). The nose solution, Eq. (24), is applied in the range $[0, \xi_0]$. The body solution is given by Eq. (23). At the back of the bubble, the liquid fraction after the hydraulic jump, $\alpha_{L2}$, is determined using Eqs. (26) and (27). When $\alpha_{L2}$ is smaller than 1, the tail shape is finally determined by Eq. (28). The position of the hydraulic jump is determined from iterative process to match the prescribed bubble volume.

The model was compared with experimental data at different liquid velocities, from 0.5 to 1.8 m/s and with different bubble volumes, from 1.5 to 6.0 l at inlet condition. Measured values of liquid flow velocity, bubble velocity and bubble volume were used as input. Data of bubbles flowing at low liquid velocities are compared with the model in Fig. 15. The nose model fits the experimental data at lower velocities, as expected, when a 'Benjamin bubble' is observed. The body solution is not able to predict the wavy interface, but it predicts successfully its average height. Eqs. (26) and (27) give a good prediction of the hydraulic jump intensity at the back of the bubble and the tail shape is very well described by Eq. (28). The model is able to capture the relationship between the jump position and the tail length. For each flow condition, when the body of the bubble is shorter, the film hold-up at the back end of the bubble is higher. The hydraulic jump is then weaker and it creates a longer tail (Fig. 15a–d).

At high liquid velocities (Fig. 16c–d), when the bubble nose moves toward the centre of the pipe, the model slightly underpredicts the liquid film hold-up at distances shorter than 20 times the pipe diameter. For longer bubbles, however, the model solution converges asymptotically to the measured shape. Fig. 17 compares the predicted and measured positions of the hydraulic jump at the back of the bubble. It shows that the model uncertainty to predict the bubble length is about $\pm 5\%$.

## 6. Shape analysis

The present analysis is based exclusively on the nose and body solutions, given by Eqs. (23)–(25). Air and water two-phase flow is assumed and Eq. (15) applies.

### 6.1. Model sensitivity

For given gas and liquid, the shape of the gas bubble depends on three parameters: $\alpha_{L\infty}$, $Fr_R$ and $f_{L0}$. The friction factor is rather constant for given liquid and pipe diameter, within a

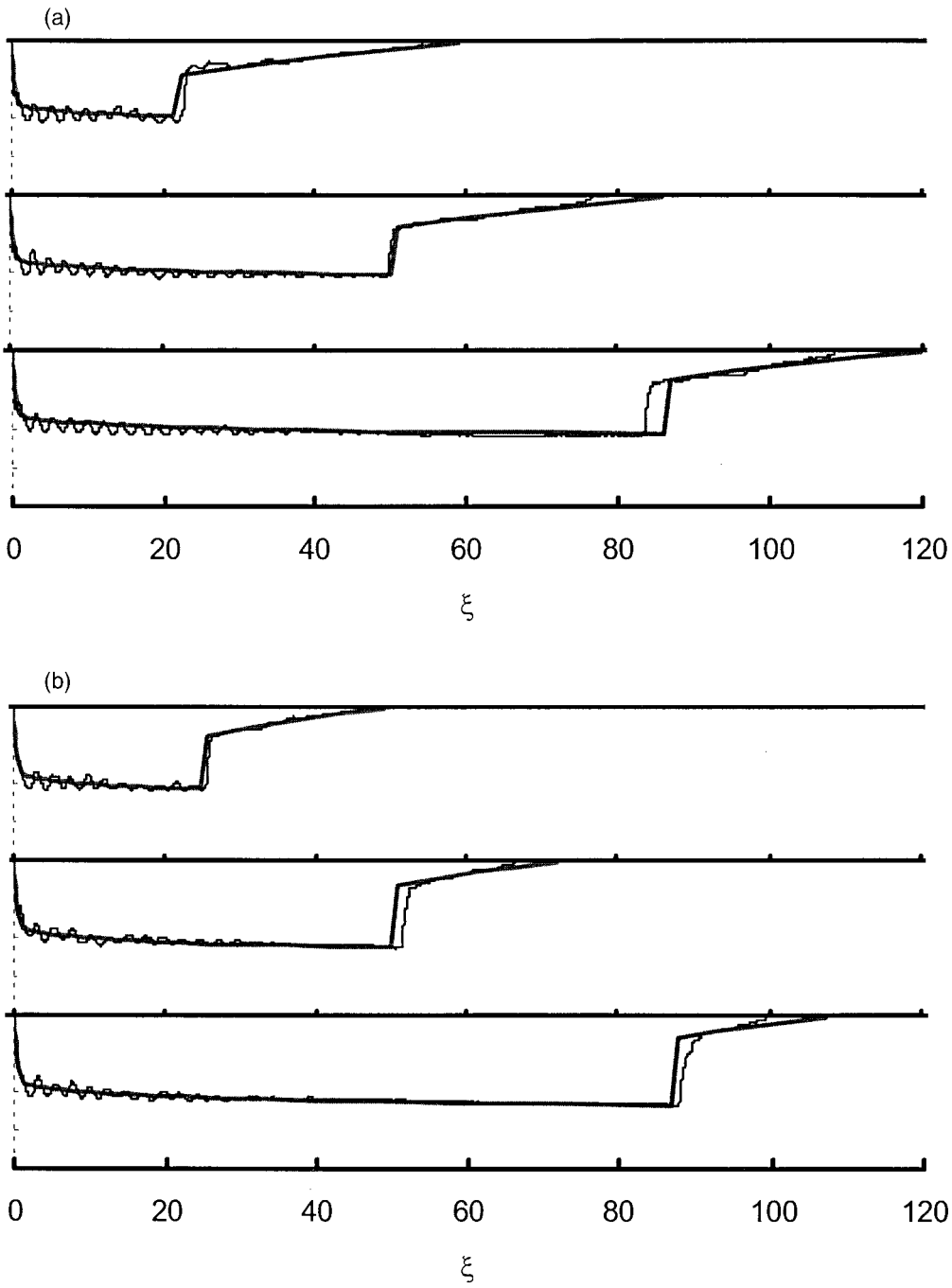


Fig. 15. Model validation: low liquid flow rates: (a) 0.5 m/s, (b) 0.6 m/s, (c) 0.7 m/s, (d) 0.8 m/s. ——— Exp. data; ——— Model.

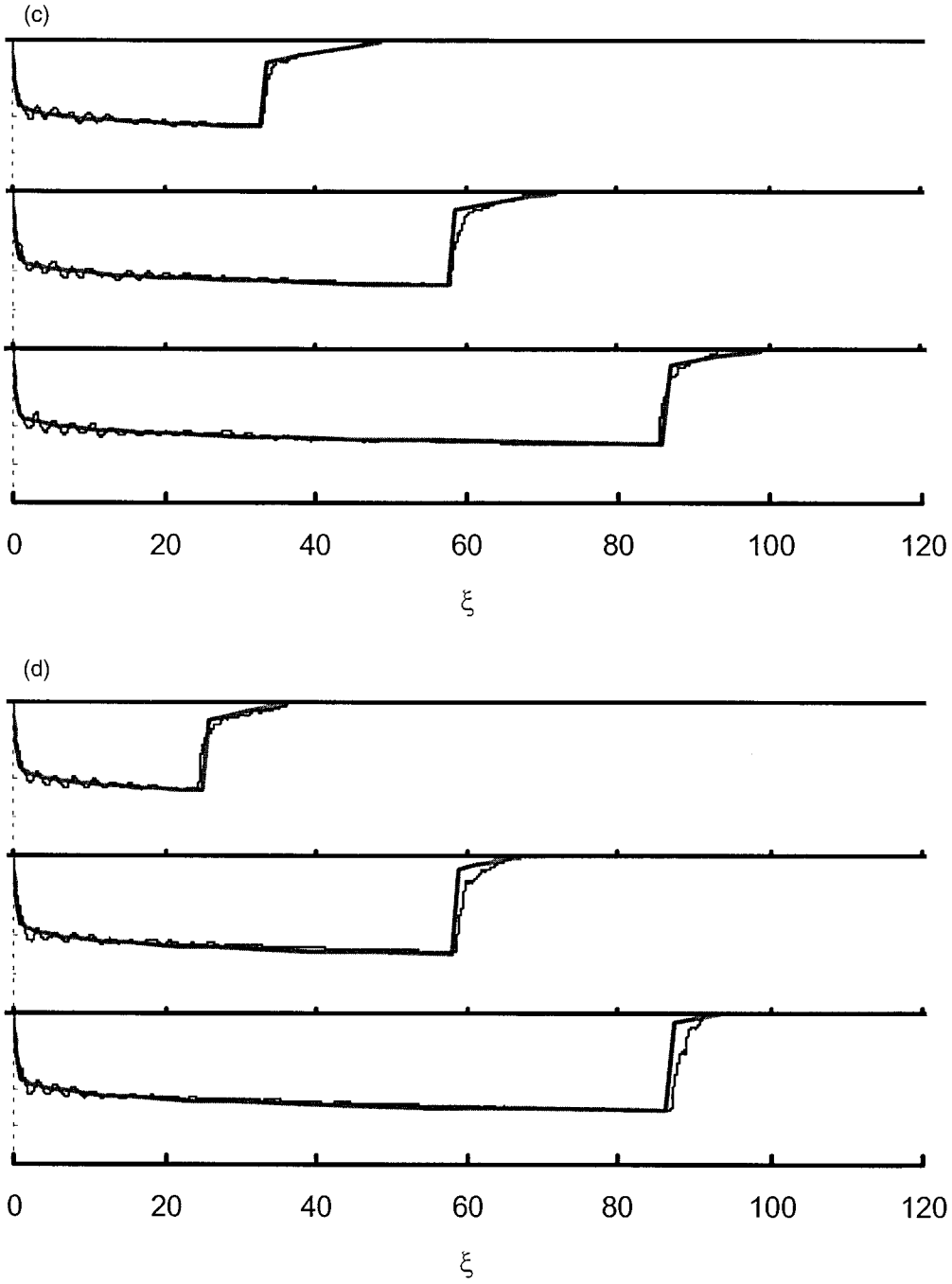


Fig. 15 (*continued*)

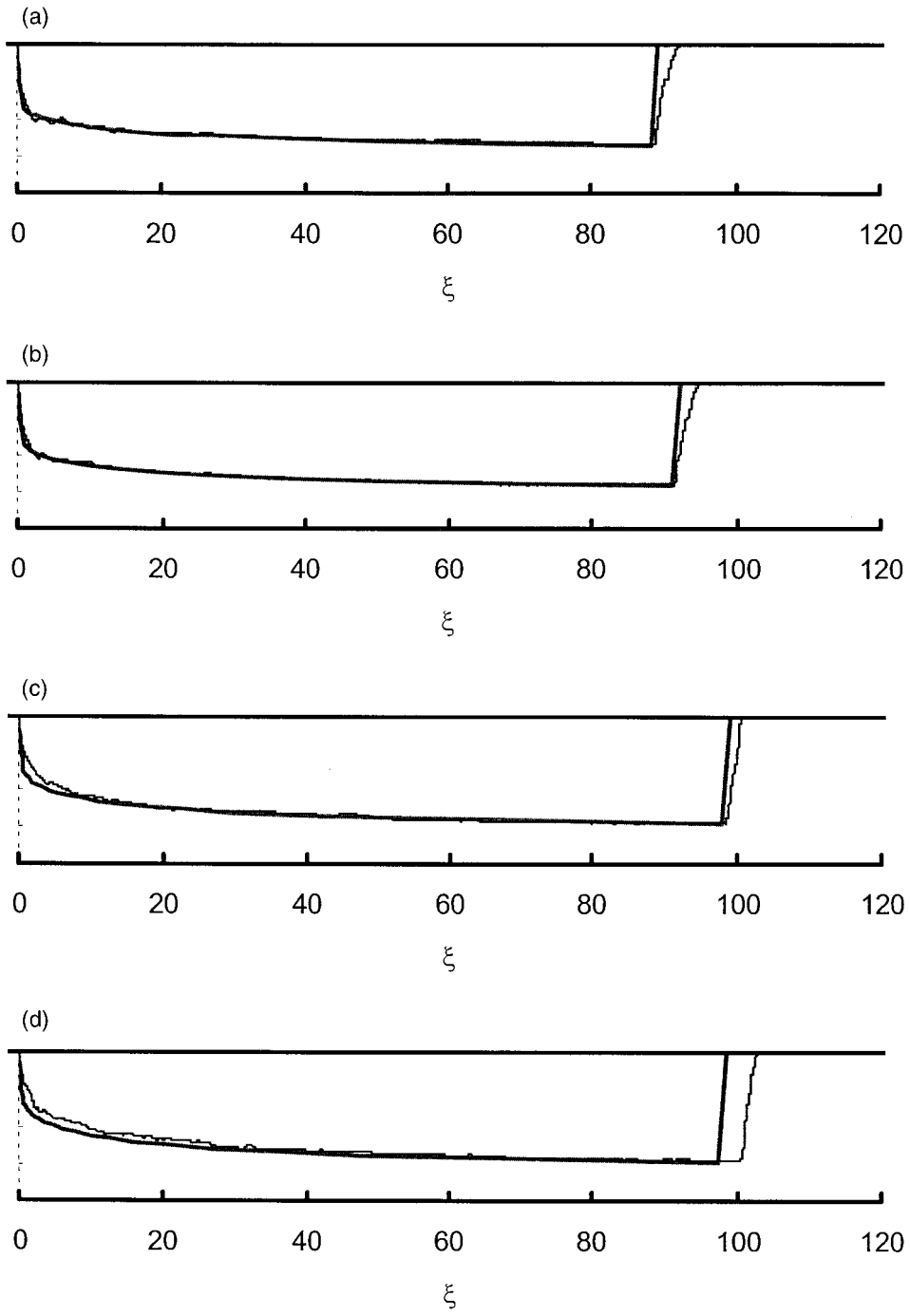


Fig. 16. Model validation: high liquid flow rates: (a) 1.0 m/s, (b) 1.2 m/s, (c) 1.5 m/s, (d) 1.8 m/s. ——— Exp. data; ——— Model.

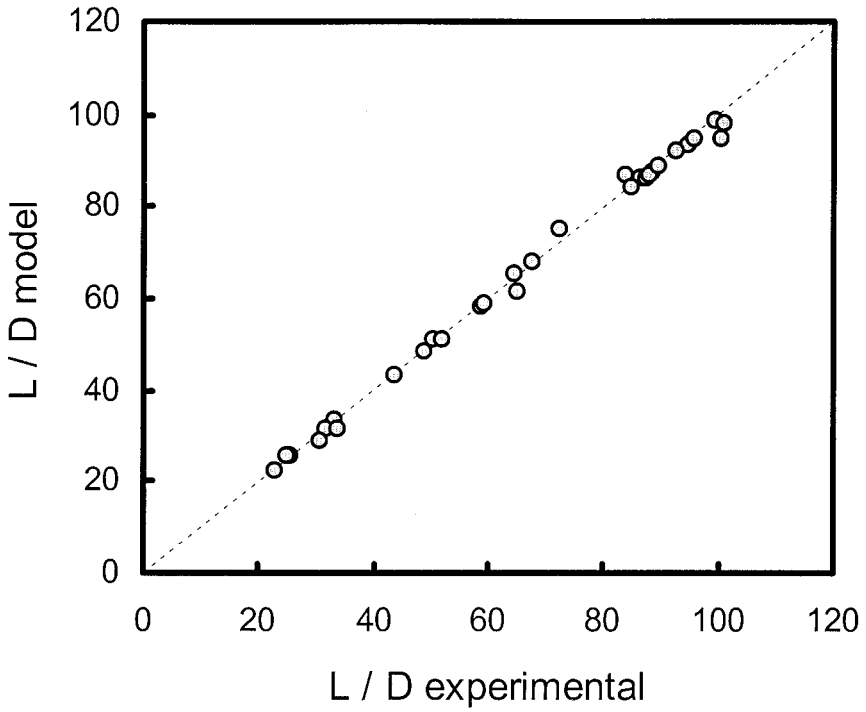


Fig. 17. Level jump position: comparison between model and experimental data.

reasonable range of the liquid velocity. Therefore, the analysis will be focused on $\alpha_{L\infty}$ and $Fr_R$. Two different situations shall be distinguished, with application to the present case ($Bo = 390$):

1. *Low liquid velocities*: For small liquid Froude number, the bubble velocity is determined by

$$V = U + 0.48\sqrt{gD}$$

In this case, $Fr_R$ is constant and equal to 0.48 while, $\alpha_{L\infty}$ is a function of $\varphi/V$ and depends on the liquid flow rate.

In this range, the liquid volume fraction far from the nose changes with the flow rate, as shown in Fig. 18. Accurate values of the velocities $U$ and $V$ are required to achieve a good prediction of the bubble length.

2. *High liquid velocities*: At high liquid Froude number, the drift term vanishes and the bubble velocity is determined by

$$V = 1.2U$$

In this case, $Fr_R$ depends on the liquid flow rate and $\alpha_{L\infty}$ is constant and equal to 0.173.

The liquid fraction far from the nose does not depend on the flow rate. Fig. 19 shows that the shape near the nose varies with the liquid velocity but far from it, the shape is independent of the flow conditions. In this case, a reasonable estimation of the phase velocities allows a good prediction of the bubble length.

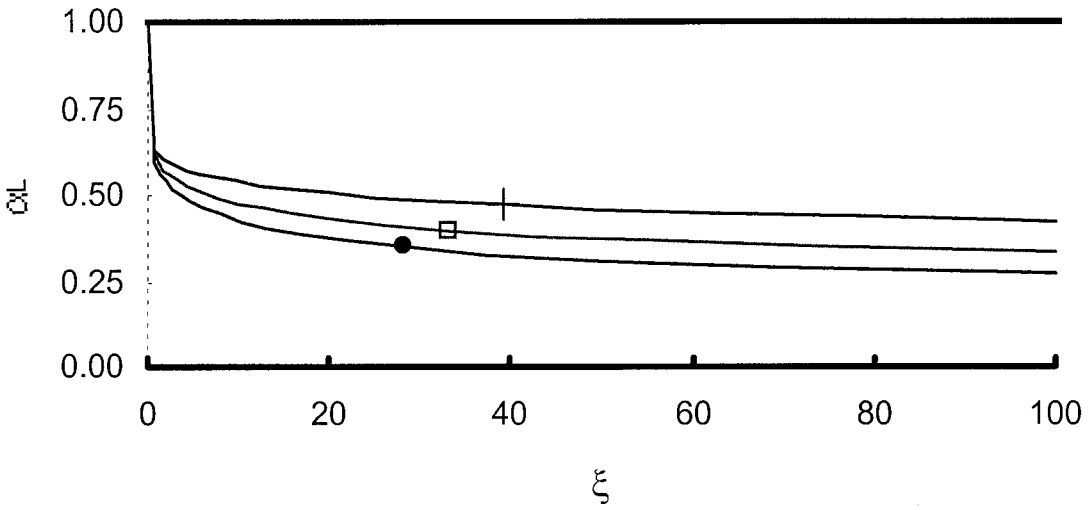


Fig. 18. Shape at low flow rates: $Fr_U = +$ 1.0; □ 1.5; • 2.0.

### 6.2. Mean void fraction at the bubble region and fully developed liquid film

The slug tracking codes usually estimate a mean gas volume fraction to determine the bubble length. Fig. 20 shows, for different values of $Fr_U$, the evolution of the ratio between the mean void fraction and the void fraction far from the nose, versus the bubble length. Even for bubbles as long as $200D$, the film cannot be considered fully developed. For a bubble of $40D$ and when $Fr_U$ equals 3, the use of $\alpha_{L\infty}$ as the mean void fraction underpredicts the bubble length of about 25%. At higher velocities the same figure shows that this error increases.

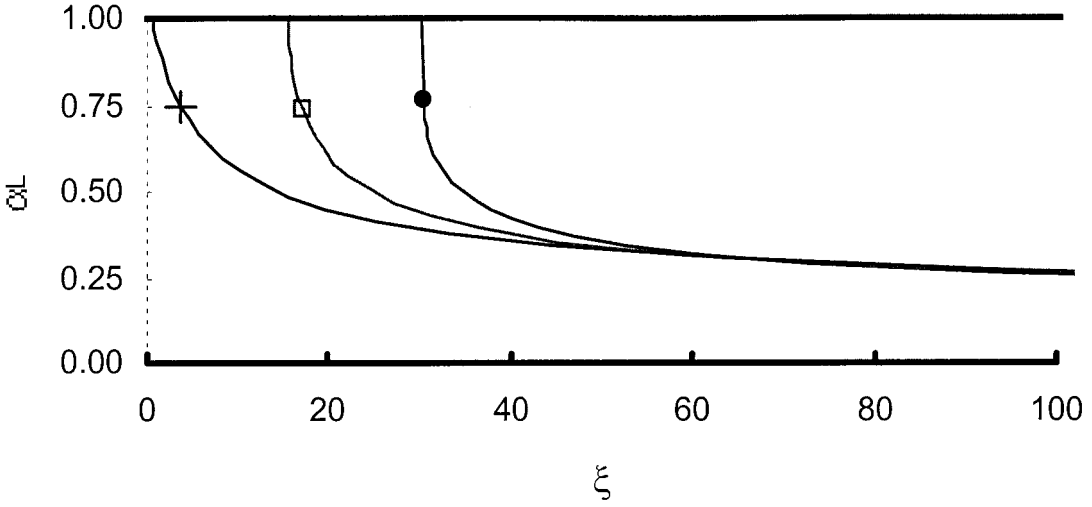


Fig. 19. Shape at high flow rates: $Fr_U =$ • 3.0; □ 5.0; + 10.0.

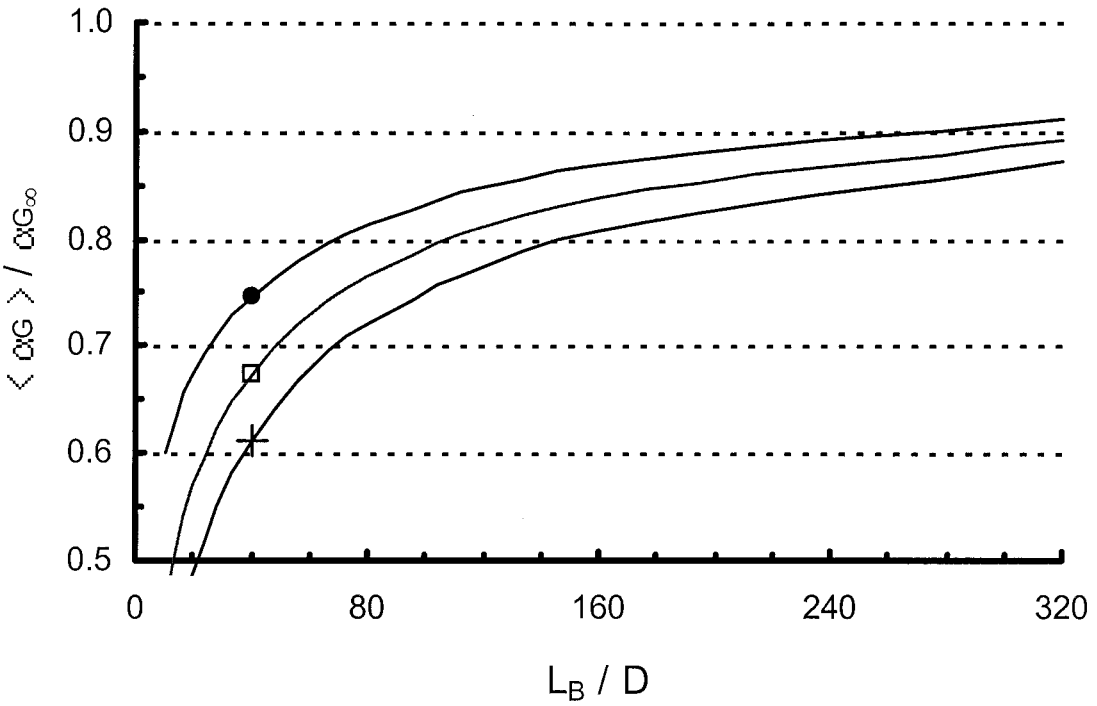


Fig. 20. Ratio between the actual mean void fraction and the void fraction of a bubble of infinite length: $Fr_U$ = • 3.0; □ 5.0; + 10.0.

Fig. 21 shows the length for a bubble to have a mean gas fraction equal to 90% of the gas fraction of a bubble of infinite length. Only bubbles longer than 200$D$ reach this percentage.

## 7. Conclusion

The shape of long isolated bubbles moving in a horizontal liquid flow was measured using a set of liquid height sensors. Liquid velocities ranged from 0.5 to 1.8 m/s and bubble volumes varied from 1.5 to 6.0 l at inlet condition. The measured liquid height of the film was converted into volume fraction assuming a horizontal interface. A staircase shape was observed at liquid velocities smaller than 0.8 m/s.

A model to predict the bubble shape and its length is proposed. The bubble length is a function of the pipe diameter, the velocity of the liquid moving ahead of the bubble, the bubble velocity and its volume. The model may be easily integrated into slug tracking codes and it agrees with experimental data.

Based on the model and on experimental data, a staircase shape is always observed when the mixture Froude number, $Fr_U$, is less than 1. For $Fr_U$ between 1 and 3, the existence of a tail behind the bubble depends on the length of the bubble body.

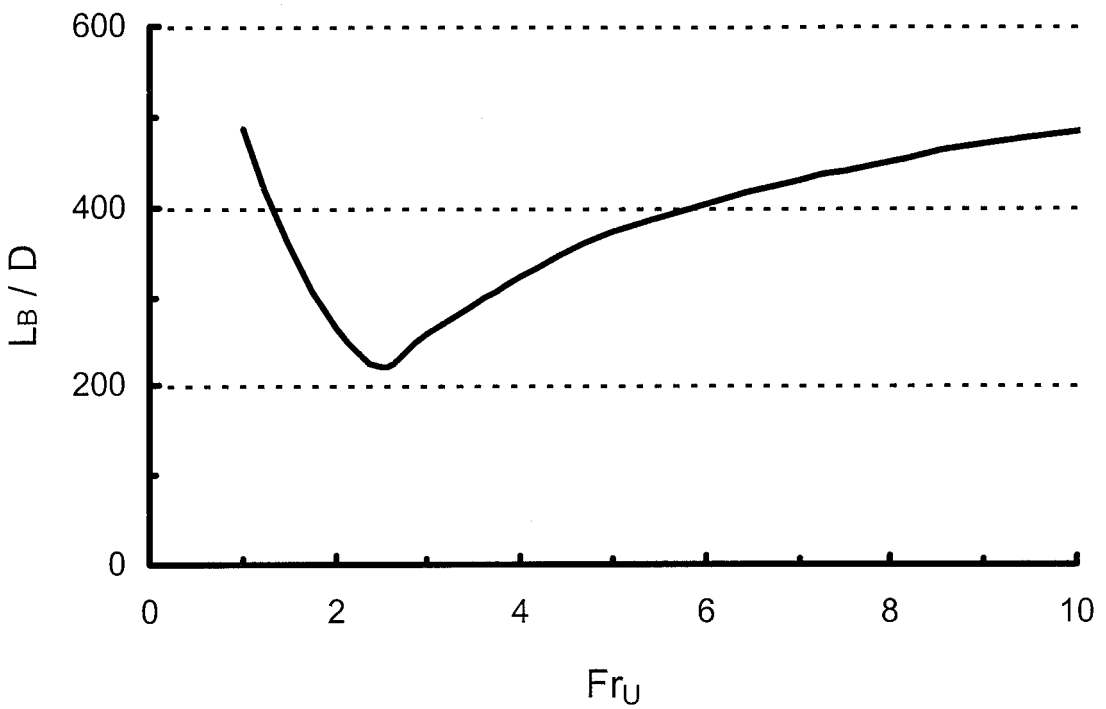


Fig. 21. Length of bubbles where $\langle \alpha_G \rangle = 0.90\alpha_{G\infty}$

In usual slug flow models that aim to predict the void fraction, the assumption of fully developed liquid film under the long bubbles tend to overestimate the gas fraction in this part of the slug structure. The liquid film under bubbles shorter than 200 times the pipe diameter is never fully developed.

## Appendix A. Geometric relations in a circular section

Referring to Fig. A1, the internal angle $\theta$ may be written as:

$$\theta = 2\cos^{-1}(1-2h), \quad \text{where } h = \frac{H}{D}$$

The liquid volume fraction is then:

$$\alpha_L = \frac{\theta - \sin\theta}{2\pi}$$

The wetted perimeter $S_L$ and the interface perimeter $S_I$ are, respectively:

$$S_L = \frac{\theta D}{2} \quad \text{and} \quad S_I = D\sin(\theta/2)$$

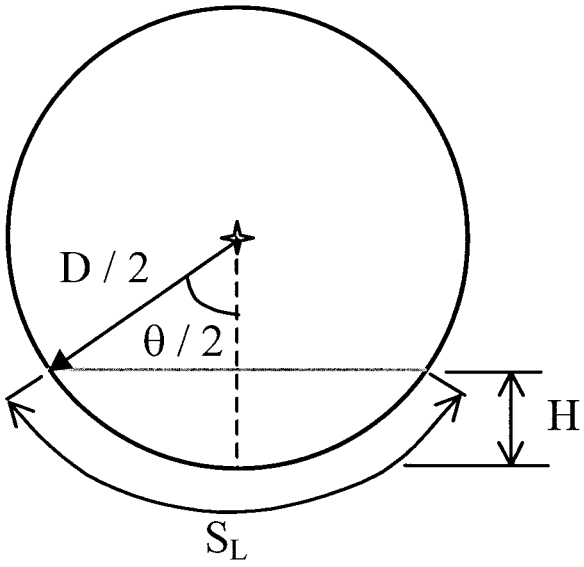


Fig. A1. Geometric relations.

A non-dimensional perimeter may be defined as the ratio between a perimeter and the total pipe perimeter:

$$s_L = \frac{S_L}{S} = \frac{\theta}{2\pi} \quad \text{and} \quad s_I = \frac{S_I}{S} = \frac{\sin(\theta/2)}{\pi}$$

It is obvious that for the gas phase one may write:

$$\alpha_G = 1 - \alpha_L \quad \text{and} \quad s_G = 1 - s_L$$

Fig. A2 shows the evolution of $s_L$ with the liquid fraction. When $\alpha_L$ varies between 0.2 and 0.8, $s_L$ may be approximated by a linear expression:

$$s_L = \frac{\alpha_L + 0.5}{2}, \quad 0.2 < \alpha_L < 0.8$$

The expression for $(dh/d\alpha_L)$ may be deduced:

$$\frac{dh}{d\alpha_L} = \frac{A}{D}\frac{dH}{dA_L} = \frac{\pi D}{4}\frac{1}{S_I} = \frac{1}{4s_I} \Longrightarrow \frac{dh}{d\alpha_L} = \frac{\pi}{4\sin(\theta/2)}$$

Fig. A3 shows how $(dh/d\alpha_L)$ varies with the liquid fraction. If $\alpha_L$ is limited between 0.2 and 0.8, this parameter may be considered constant and equal to 0.820.

The function $\Phi(\alpha_L)$ is defined in the paper as:

$$\Phi(\alpha_L) = \left[\frac{(\alpha_L s_G + s_I)^4 \alpha_L (s_G + s_I)}{(\alpha_G s_L)^5}\right]^{1/7}$$

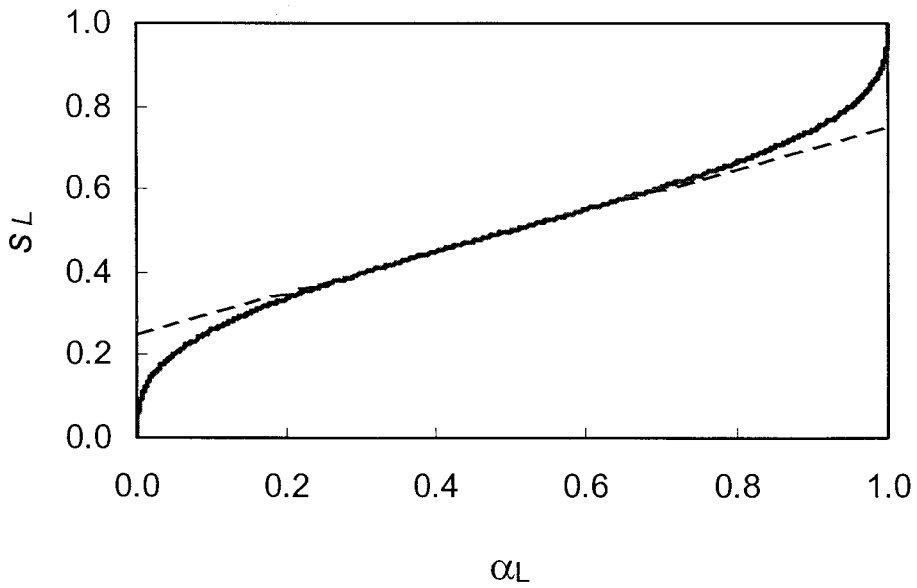


Fig. A2. Evolution of the wetted perimeter with the liquid volume fraction ——— Exact value; ——— $s_L = 0.5(\alpha_L + 0.5)$.

It is plotted in Fig. A4. When the liquid fraction is limited between 0.1 and 0.5, $\Phi$ is linearly proportional to $\alpha_L$. The linear relation shown in the figure is given by:

$$\Phi(\alpha_L) = 1.70(\alpha_L + 0.5)$$

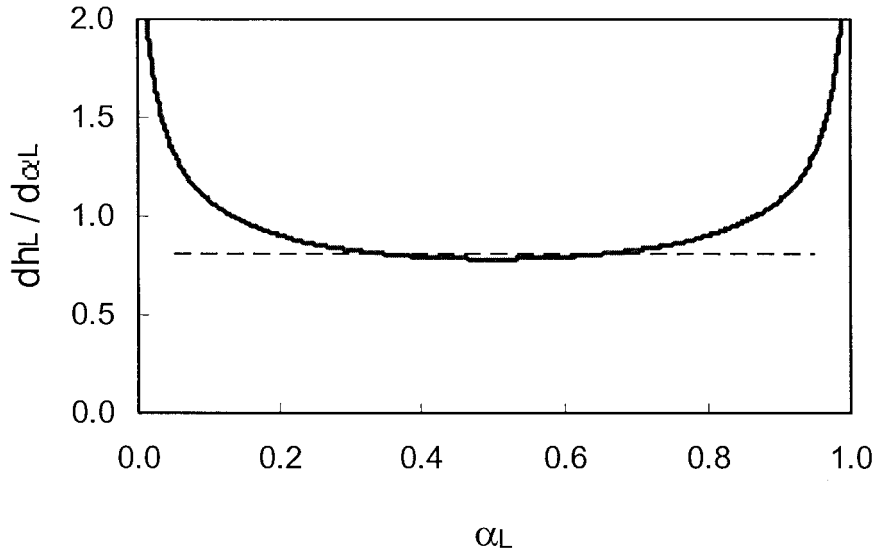


Fig. A3. Evolution of $(dh/d\alpha_L)$ with the liquid volume fraction ——— Exact value; ——— $dh/d_{\alpha L} = 0.820$.

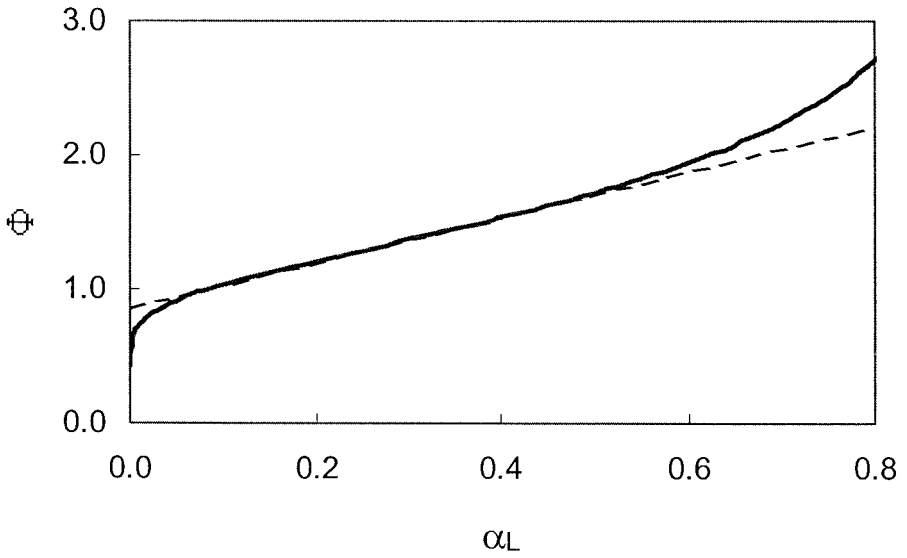


Fig. A4. Evolution of $\Phi$ with the liquid volume fraction. ——— Exact value; ———— $\Phi = 1.70(\alpha_L + 0.5)$.

## References

Andreussi, P., Bendiksen, K.H., Nydal, O.J., 1993. Void distribution in slug flow. Int. J. Multiphase Flow 19, 817–828.

Barnea, D., Taitel, Y., 1993. A model for slug length distribution in gas–liquid slug flow. Int. J. Multiphase Flow 19, 829–838.

Bendiksen, K.H., 1984. An experimental investigation of the motion of long bubbles in inclined tubes. Int. J. Multiphase Flow 10, 467–483.

Benjamin, T.B., 1968. Gravity currents and related phenomena. J. Fluid Mech. 31, 209–248.

Dhulesia, H., Bernicot, M., Deheuvels, P., 1991. Statistical analysis and modelling of slug lengths. In: Proc. 5th Int. Conf. on Multiphase Production, Cannes France, June 19–21.

Dukler, A.E., Hubbard, M.G., 1975. A model for gas–liquid slug flow in horizontal and near horizontal tubes. Ind. Chem. Fundam. 14, 337–347.

Fabre, J., Liné, A., 1992. Modelling of two-phase slug flow. Annu. Rev. Fluid Mech. 24, 21–46.

Fabre, J., Liné, A., Peresson, L., 1989. Two-fluid/two-flow-pattern model for transient gas–liquid flow in pipes. In: Proc. 4th Int. Conf. Multi-phase flow, June 19–21, Nice France, Cranfield BHRA.

Fagundes Netto, J.R., 1999. Dynamique de poches de gaz isolées en écoulement permanent et non-permanent horizontal. PhD thesis, Institut National Polytechnique de Toulouse (INPT).

Grenier, P., 1997. Evolution des longueurs de bouchons en écoulement intermittent horizontal. PhD thesis, Institut National Polytechnique de Toulouse (INPT).

Grenier, P., Fabre, J., Fagundes Netto, J.R., 1997. Slug flow in pipelines: recent advances and future developments. In: Proc. Eighth Int. Conf. on Multiphase Production, June 18–20, Cannes, France, Cranfield BHRG.

Nydal, O.J., Andreussi, P., 1991. Gas entrainment in a long liquid slug advancing in a near horizontal pipe. Int. J. Multiphase Flow 17, 179–189.

Nydal, O.J., Banerjee, S., 1995. Object oriented dynamic simulation of slug flow. In: Proc. Second Int. Conf. Multiphase Flow, April 3–7, Kyoto, Japan.

Nydal, O.J., Pintus, S., Andreussi, P., 1992. Statistical characterisation of slug flow in horizontal pipes. Int. J. Multiphase Flow 18, 439–453.

Ruder, Z., Hanratty, T.J., 1990. A definition of gas–liquid plug flow in horizontal pipes. Int. J. Multiphase Flow 16, 233–242.

Straume, T., Nordsven, M., Bendiksen, K., 1992. Numerical simulation of slugging in pipelines. Multiphase Flow in Wells and Pipelines, ASME 1992 FED 144, 103–112.

Wallis, G.B., 1969. One Dimensional Two-Phase Flow. McGraw-Hill, New York.

Weber, M.E., 1981. Drift in intermittent two-phase flow in horizontal pipes. Can. J. Chem. Eng. 59, 398–399.

Woods, B.D., Hanratty, T.J., 1996. Relation of slug stability to shedding rate. Int. J. Multiphase Flow 22, 809–828.